Testing Megacam with SNDICE (revised 2013)

E Barrelet

Laboratoire de Physique Nucléaire et de Hautes Énergies

CNRS - IN2P3 - Universités Paris VI et VII

Testing Megacam with SNDICE (revised 2013)

E. Barrelet,

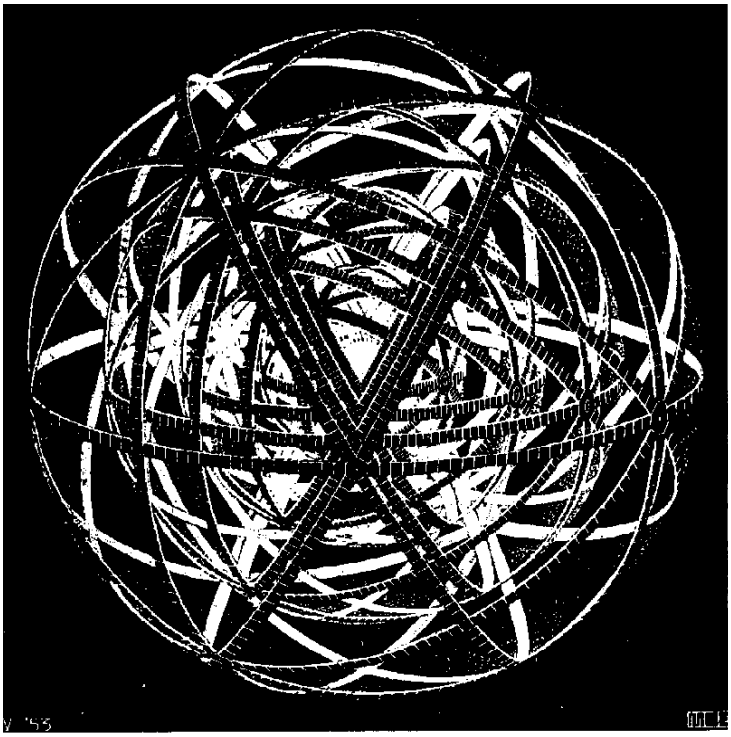

4, Place Jussieu - Tour 33 - Rez-de-Chaussée
75252 Paris Cedex 05
Tél.: 33(1) 44 27 63 13 - FAX: 33(1) 44 27 46 38

•

1 Introduction

We have gathered in this report the studies of the Megacam images produced by the SNDICE led light source. Other reports are dedicated of the study of this light source using a spectrophotometric test bench equipped with two large area photodiode detectors.
A first report[1] was issued in year 2010. More data was taken in 2010 and 2011 and many issues were clarified and presented in Augustin Guyonnet thesis[2]. This paper is an update of both.
The general goal of our tests, is to design a methodology to transfer the precision of a SNDICE light source to the CFH telescope and its megacam CCD camera.
Several limits constrained our tests. First the CCD camera could not be separated from the telescope forbiding a study of specific CCD properties. Secondly the computer control of the SNDICE light source was not integrated to the general telescope control and therefore calibration operations could not be automatized. Lastly the stability of Megacam electronics was not sufficient to take full advantage of stability of the light source. For that reason a large part of the work presented here was done in order to understand and to mitigate the electronic malfunctions, up to the point where the response of the whole telescope is seen as compatible with the 10^{-4} precision of our SNDICE emission model.
In particular, with SNDICE in a fixed position relatively to the telescope, the flux can be programmed very precisely either by fixing the exposure time (electronically or mechanically) or the LED current (here again SNDICE flux is controlled at a $\sim 10^{-4}$ precision).
For this reasons our study is based on data taken during two years in a sequence of 11 runs taken either at varied exposure duration or at varied flux, with the light source at a fixed position relative to the telescope.

2 Methods used for the analysis of Megacam images

2.1 Data structure

A Megacam raw data image is made of 72 ‘amplifier’ blocks numbered k=0 to 71. The two amplifier channels belonging to the same CCD are numbered by an even number followed by the next odd number. The CCD are numbered from k’=0 to 35 as shown in Figure 1, hence the channels are numbered from 0 to 71 (or from 1 to 72). Each image block, as in Figure 2, contains 1024*4611 real pixels and a few dummy ‘overscan’ pixels extending the line size to 1056 pixels (electrons traversing the full serial register during one line readout) and extending the number of lines to 4644 (electrons traversing the full image area during the image readout period). The image area will be limited to 1024*4608 pixels by suppressing the last three lines, in order to exploit a 2*9 block structure (a “superpixel” block is a 512*512 pixel array). The area covered by a given channel is covered by two “supercolumns” and nine “superlines”.
Each overscan area is divided in two bands: band 1 contains trailing charges left over from the exposure and band 2 contains a cleaner ‘pedestal’. The double overscan area (x>1028 and y>4619) contains therefore the cleanest ‘pedestal’. It is for all images a constant as

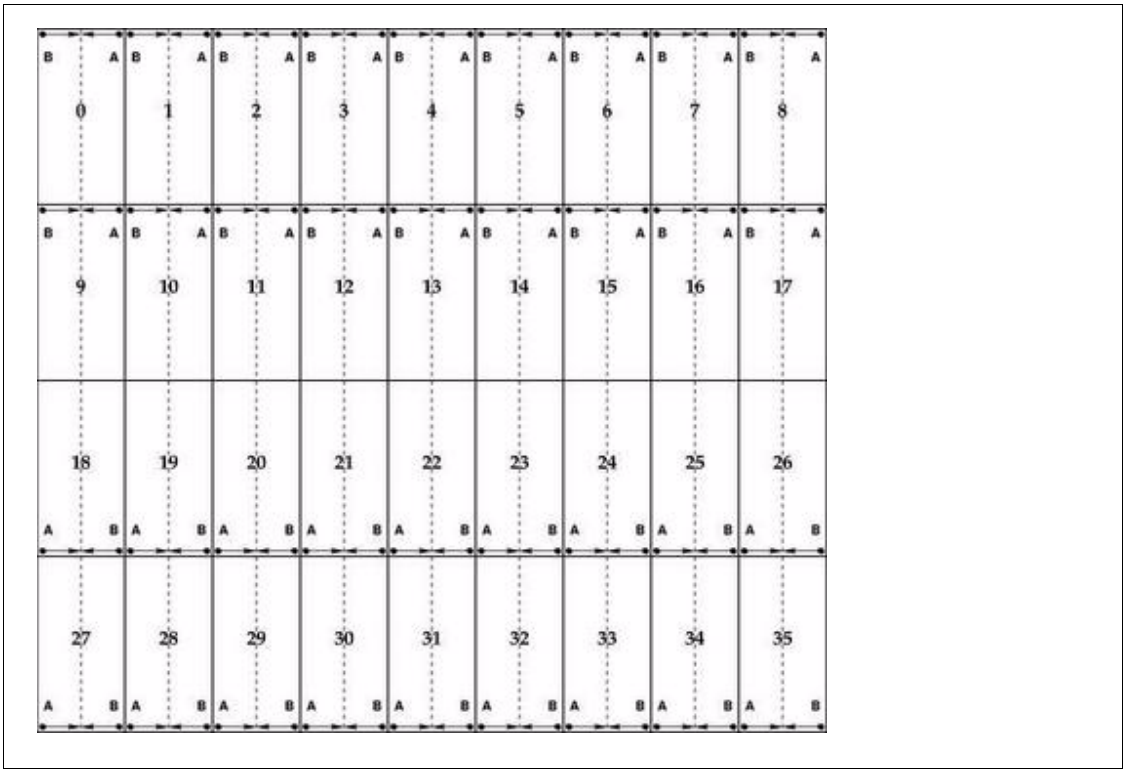

Figure 1: Megacam CCD numbering scheme (*k'* =0-35). The two channels A and B on each CCD are situated in a corner and the nearest pixel is read first (pixel (col=1; line=1). The channel number is *k*=2**k'*+0 (left amp) or *k*=2**k'*+1 (right amp).

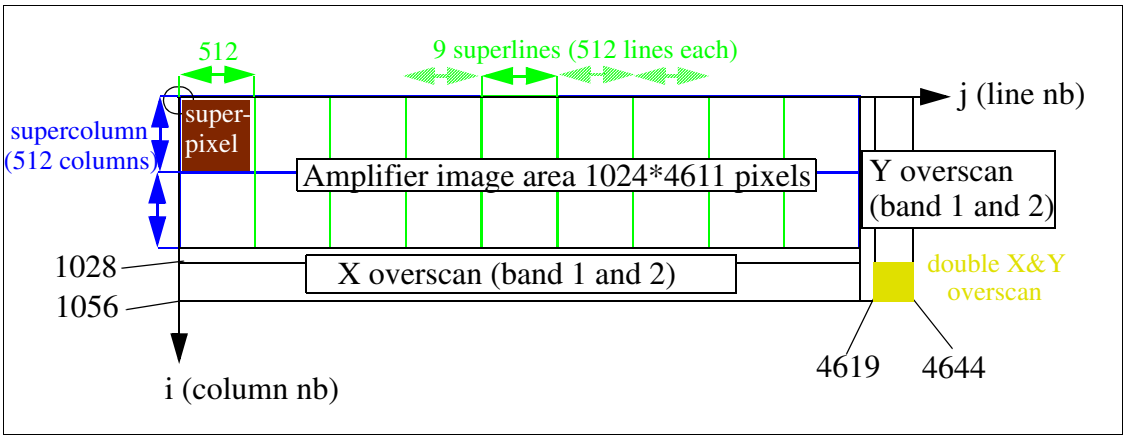

Figure 2: Organization of the pixel array corresponding to one channel (two channels per CCD)

shown in Figure 3-a). The average $O_{k,I}$ for image I and for channel k of the 28*25 double overscan pixels is the best definition of a pedestal that we have found. Its gaussian error is around 0.1 adu (pixel noise/$\sqrt{28 \times 25}$). In the following we shall subtract systematically the number $O_{k,I}$ to the adc content of each pixel and call the result the global pedestal subtracted image.

The value of these global pedestals is not very stable in the short time scale, as seen in Figure 4 .. It is even more unstable in the long time scale. Their variations are two order

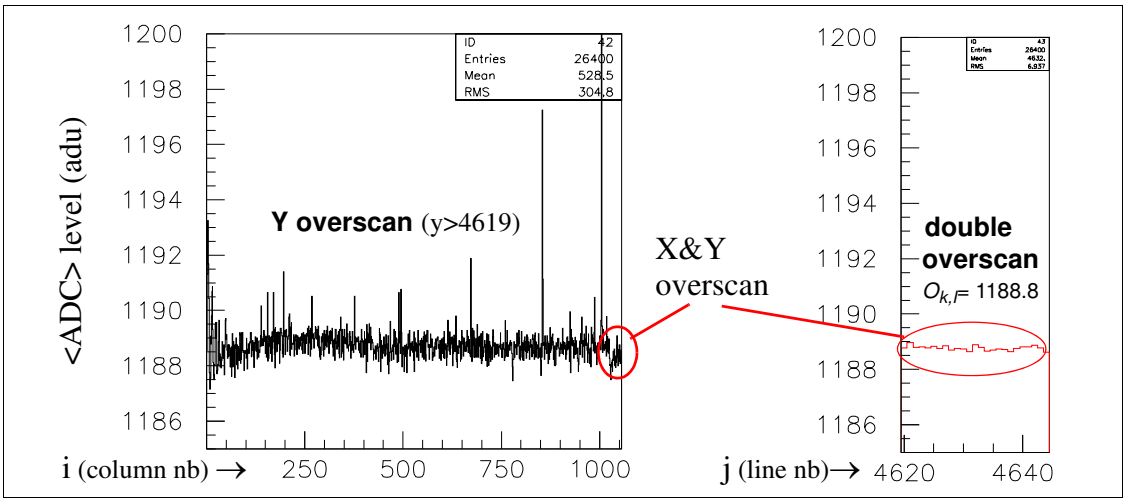

Figure 3: Y overscan (band 2): a) a whole X profile (averaged in y); b) corresponding Y profile (averaged in x) of double overscan (25 pedestal samples with 0.5 adu rms each). $O_{k,I}$ is the double average (in x and y).

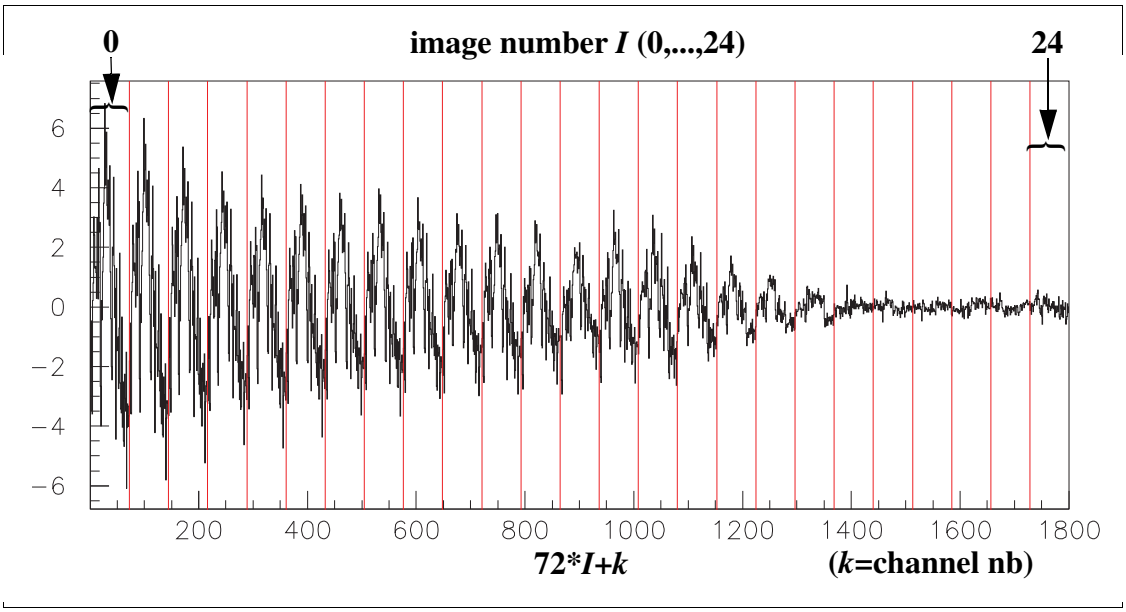

Figure 4: Variation of Megacam pedestals $O_{k,I}$ -$O_{k,ref}$ for 25 images taken during a half hour. For each image ***I***, the channel number ***k*** is varied from 0 tà 71. For each channel, the variation is relative to a reference (a mean of the 6 last images).

of magnitude larger than have been observed in similar electronics. This instability is a first manifestation of the many problems encountered in reading Megacam images.

2.2 Modeling the instability of the electronics

By construction the CCD readout electronics is an electrometer. It should yield a null value for all pixels of a dark frame after pedestal subtraction, except for a minimal positive value due to the thermal dark current electrons and the Gaussian white noise. This is by definition what an electrometer measure by using a two step operation:
a- nulling the input charge, **b**- transfering the charge to be measured on the input. This

operation is usually called “correlated double sampling”. Its implementation in the Megacam electronics is described in Appendix A. This Appendix A refers to a R&D study (Claire Juramy’s thesis) showing that one can get a bias null in average (after pedestal subtraction) with a 0.1 adu precision and a Johnson noise <2 adu RMS (eventually plus a 0.5 adu KT/C noise due to Megacam clamping) and a gain stability better than 10^{-4}.
Contrary to this almost ideal system, we shall see in this section that in the Megacam system some extra noise sources yield a pedestal variations larger than 20 adu.
The second characteristic of an ideal electrometer is a fixed gain (adu/charge) which is the same for all electric charges measured with a given preamp. We shall show in the following sections, that the gain of Megacam electronics is also not ideal with fluctuations of 1% instead of a few 10^{-5} for a ideal system.
These problems in the Megacam electronics could wreck our analysis of the Sndice intrinsic stability and affect seriously some astronomical measurements. We have investigated how to mitigate their effects and how to check that the 10^{-4} precision of Sndice is there, under this noise.
This analysis will be resumed by the 2 modeling the behaviour of Megacam electronics with additive parameters (“pedestal”) and with multiplicative ones (“gain”). The former parameters are deduced from the analysis of sequences of “bias frames” (section) and the latter from “constant level” or from “level ramp” sequences of images (section). More complex but smaller effects are also seen in overscan part of level ramp images (cf. “baseline shift”).

2.3 Bias frames

Bias (or dark) frames are CCD images taken with shutter closed and with readout started immediately (or a few seconds) after the CCD erasure. In fact it is not correct to call them “bias frames” because correlated double sampling and pedestal subtraction should null the bias and suppress the noise added to it.
Typical parasitic effects studied here are seen in a megacam bias frame such as seen in Figure 5..
We performed the analysis of a set of 62+16 frames taken during the Sndice runs used for this report distributed in 10+1 different months (more than 5 frames for each run).
We observed characteristic bias profiles depending either on the column number **X** or independently on the line number **Y**, at the level of ten adus (cf. Figure 6). These residual biases affect equally the image area and the overscan areas. They prove that the electronic is not working as it should.
The X and Y profiles of different channels are different as one can check at http:// supernovae.in2p3.fr/~barrelet/megadice.html.
The X profiles are very stable and are dominated by the electronic gaussian white noise (~2.5 adu /pixel and ~0.05 adu/column, cf.Figure 7). They follow a damped 40μs oscillation pattern.
The Y profiles can vary enormously within a few hours as shown in Figure 8. However they vary little from one line to the next (less than 0.2 adu, cf. Figure 9) but a lot more

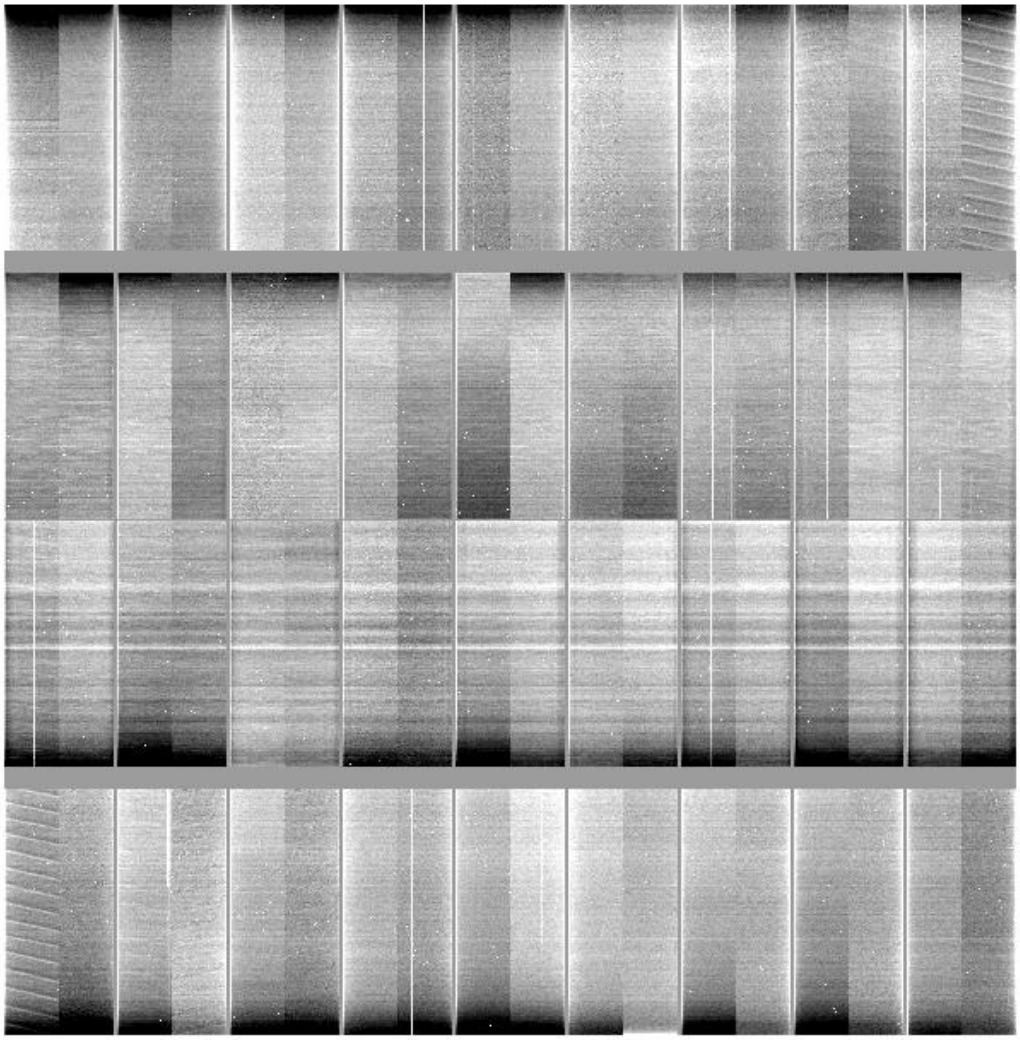

Figure 5: Typical bias frame : 50hz noise gives inclined stripes (upper right and lower right); microphonic noise yield horizontal stripes in third CCD row from the top; dark areas due to Y profile seen in Figure 6.

at a 30 lines intermediate frequency (likely from microphonic noise) and from one frame to the next. Our resulting policy is to select carefully the reference frames for each run and to characterize the Y profile for each preamp as the year average of reference frames. For plain flat field images the residual bias profiles might be lost in the photon noise but they are still clearly seen in overscan regions. We shall systematically subtract these profiles as indicated in the following formula:

$$\wp_{i,j,k,I} = C_{i,k} + L_{j,k} + O_{k,I} \qquad \begin{array}{l} i = 1,1056 \\ j = 1,4644 \\ k = 0,71 \end{array} \qquad \begin{array}{l} \sigma(O_{,I}) \approx 4 \rightarrow 10^{-1} \\ \sigma(C_{,k}) \approx 4 \times 10^{-2} \\ \sigma(L_{,k}) \approx 4 \times 10^{-1} \\ \sigma(\wp_{,k}) \approx 2 \end{array} \tag{1}$$

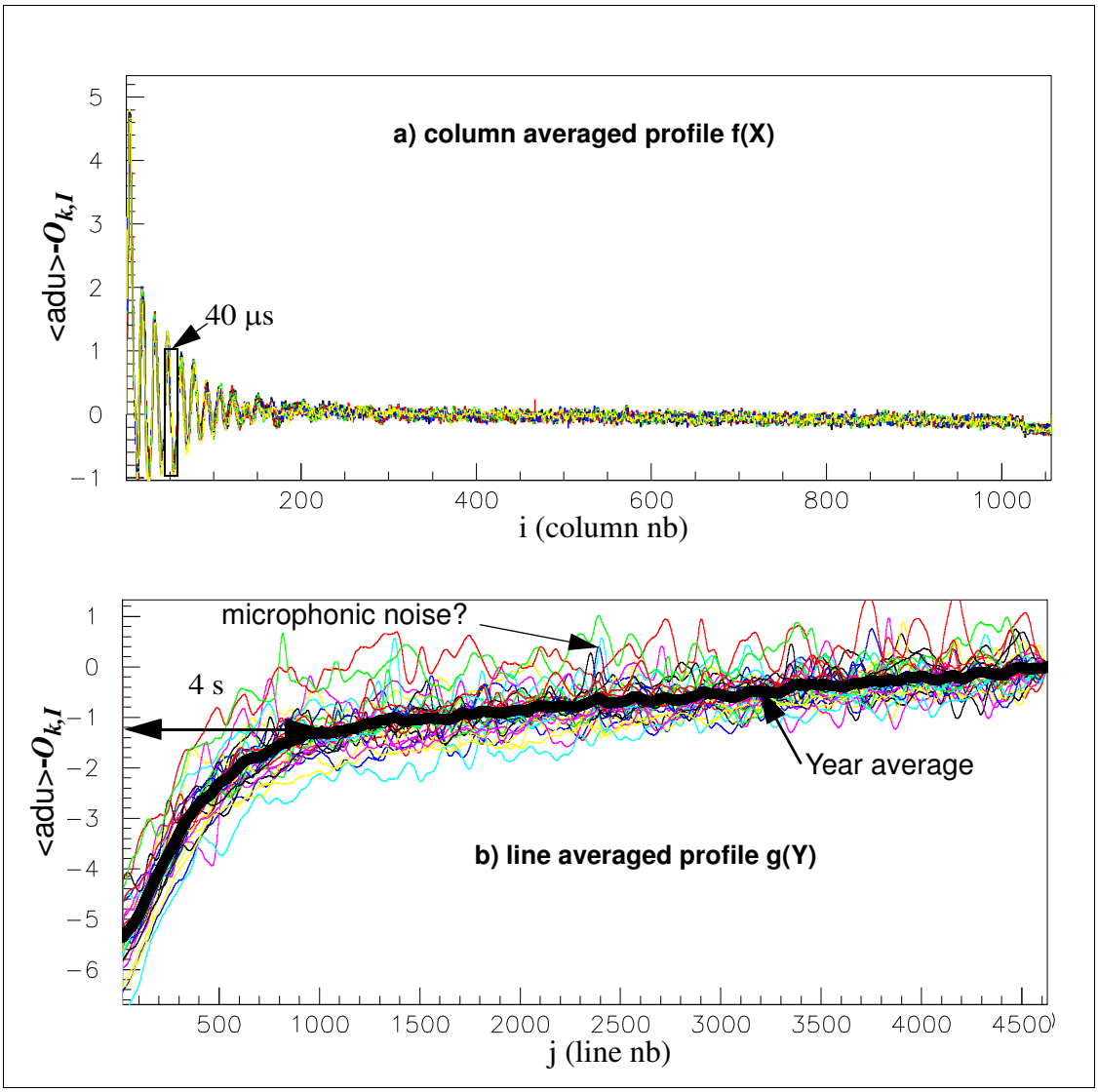

Figure 6: For a preamp, each bias (pedestal subtracted) is represented with a different color:
a) the column profile f(X) is stable during one year for 62 bias frames (typical frequency 25 kHz)
b) the line profile g(Y) is noisy and unstable from one frame to the next (typical frequency 25 Hz).

It reduces the effects of the system noise on any given pixel which can be above 10 adu's depending on the column i, the line j, the channel k and the image number I. The remaining fluctuations of a pixel $\wp$(i,j,k,I) are given in 1 in adu count.

a) The main one $O_{k,I}$ is an overall fluctuation of the bias of a given channel k from a reference image to the given image *I*. It increases (or decreases) with time during one hour for a sequence of 25 identical images between ±6 adu (cf Figure 4). This fluctuation is reduced to $\sigma(O_{k,I})$ =0.1 adu by subtracting the average of the 25x28 pixels of the double overscan region of channel k in that image *I*.

b) The pixel electronic noise $\sigma(\wp_{,k})$, due to the CCD preamplifier, to the AC coupling capacitor and to the megacam amplifier, is gaussian. It varies from 2.5 to 3 adu rms depending on the channel number k and it is very stable.

c) The column correction $C_{i,k}$ is naturally taken as the year average of the column bias f(X) shown in Figure 6. It is very stable during a year and precise, with $\sigma(C_{,k}) \approx 4\times10^{-2}$

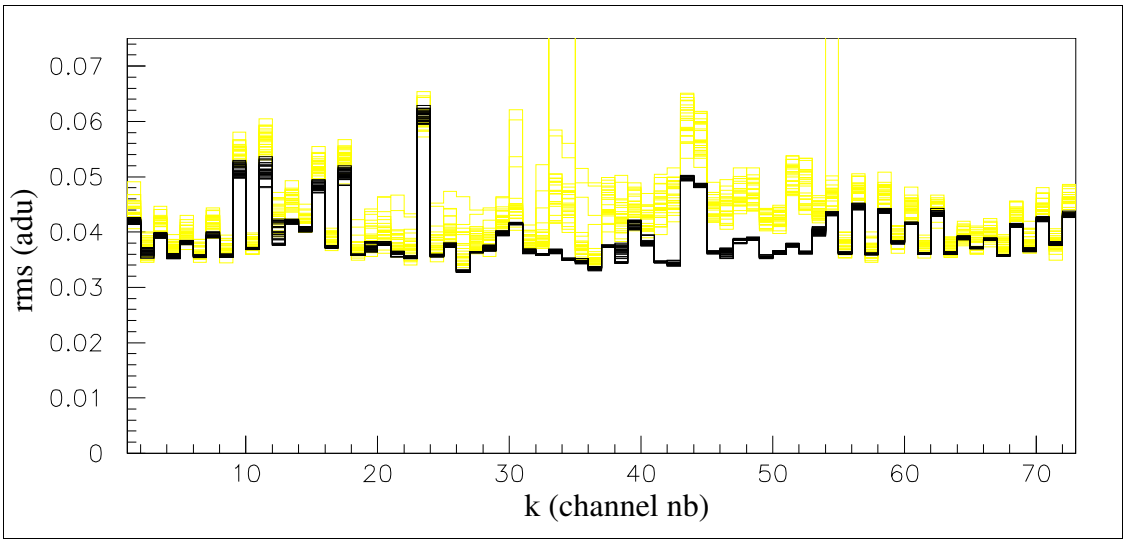

Figure 7: The noise affecting the line bias as a function of preamp number is figured by the yellow lines representing the RMS of each frame independently. It is compared to the value (in black) of "pure" electronic noise, i.e. $\sigma(\wp_k)/(\sqrt{4644})$. The black-to-yellow difference is due to system noise.

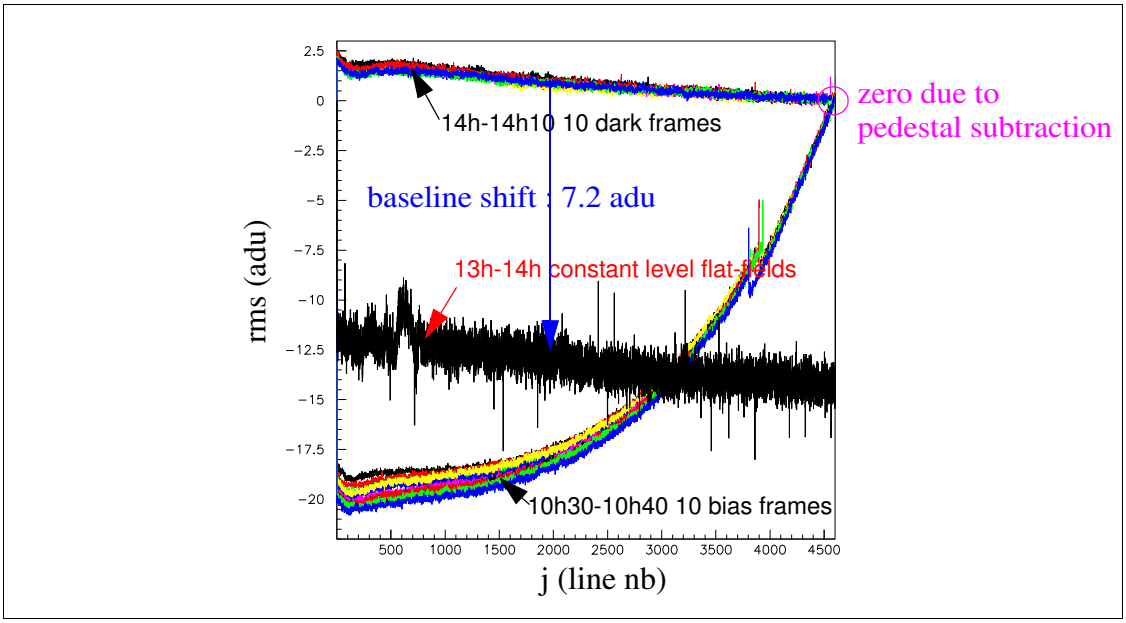

Figure 8: The Y profile instability during the run of 28/10/2008 : It jumps up by 20 adu between the first 10 bias frames of the run to the last 10 dark frames taken 3.5 hours later. These last dark frames are taken as the reference for the 25 constant level flat fields studied in section?? The 7.2 adu difference is due to the baseline shift studied in Figure 10. More generally, we have empirically selected a group of reference Y profiles for each level ramp run of our study.

as shown in Figure 7. By construction it is such as $<C_{i,k}>=0$.

d) The line correction $L_{j,k}$ is also taken as the year average of the line bias g(Y) shown in Figure 6. It fluctuates from an image to the next due to system noise as shown in Figure 9. The overall fluctuation $\sigma(L_{,k}) \approx 4\times10^{-1}$ is smaller than the pixel electronic noise $\sigma(\wp_k)$. That does not mean that it is negligible. Flux estimators such as background estimators integrate a large number of pixels and expect an average value decreasing as

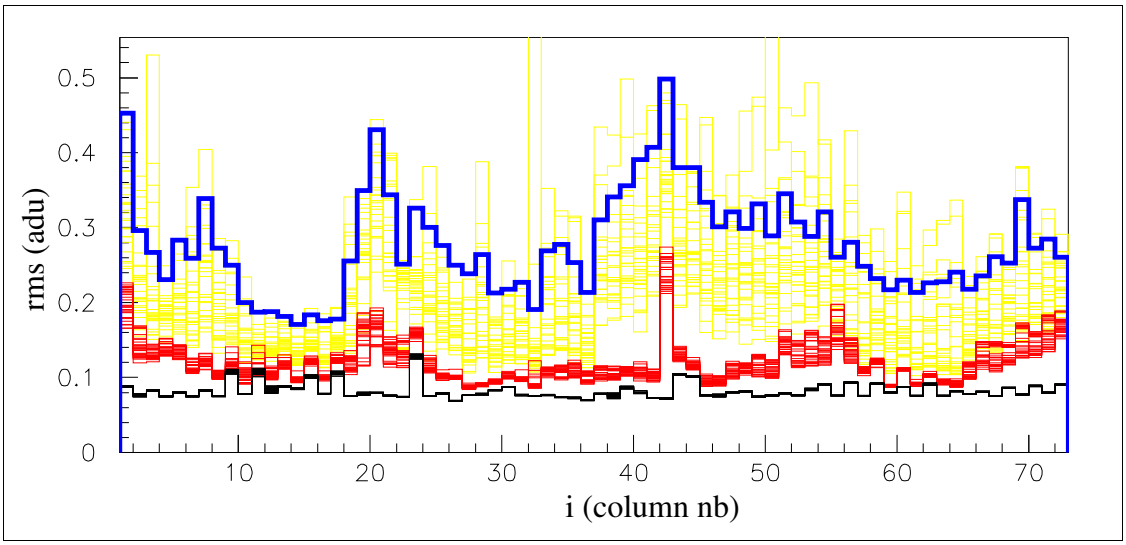

Figure 9: As in Figure 7 the black line represent the effect of "pure" electronic white noise $\sigma(\mathcal{O}_k)/(\sqrt{1056})$, while the real noise is subdivided in three frequency ranges. In red the highest line frequency (one line compared to neighbours). In yellow the intermediate frequencies represented in Figure 6 (using a sliding average filter over 30 consecutive lines). In blue all frequencies included (but subtracted from the year average).

the square root of the number of pixels. That does not work in this case.
We shall argue in Appendix A that it is possible to fine tune a CCD readout electronics such as Megacam's in order to reduce the mean values of the bias and its fluctuations below the 0.1 adu level. This would be both a huge practical gain and would also give a better performance.

2.4 Overscan regions in flat field exposures

Overscan regions are usually expected to contain essentially pedestal values. It is therefore a good check of the pedestal subtraction method. In fact it will exhibit another electronic problem: the baseline shift.

2.4.1 Y overscan

Figure 4 shows some residual electrons trailing in the Y overscan region (in particular inside a few columns which contains pixels with long lifetime traps).
The adc value in the double overscan region (X>1028 and Y>4619) does not suffer from this problem. In principle it gives the best estimate of the constant which characterizes the rest state of the electronics when the CCD is not filled nor clocked. It should be the same for all bias frames and could differ for flat field exposures due to the different load on the electronic system during the 20 s readout time. There will not be such concern here because even for bias frames that "constant" $O_{k,I}$ varies from one image to the next!

2.4.2 X overscan

At least two effects are seen in the X overscan region which affect the pedestal value (one positive and one negative).

The first effect affecting flat field images is the trailing overshoot signal seen in the band 1 of X overscan (1024<X<1029). The second effect is an undershoot seen at higher X in Figure 10-a. The depth of this undershoot is proportional to (=0.1%) the mean charge

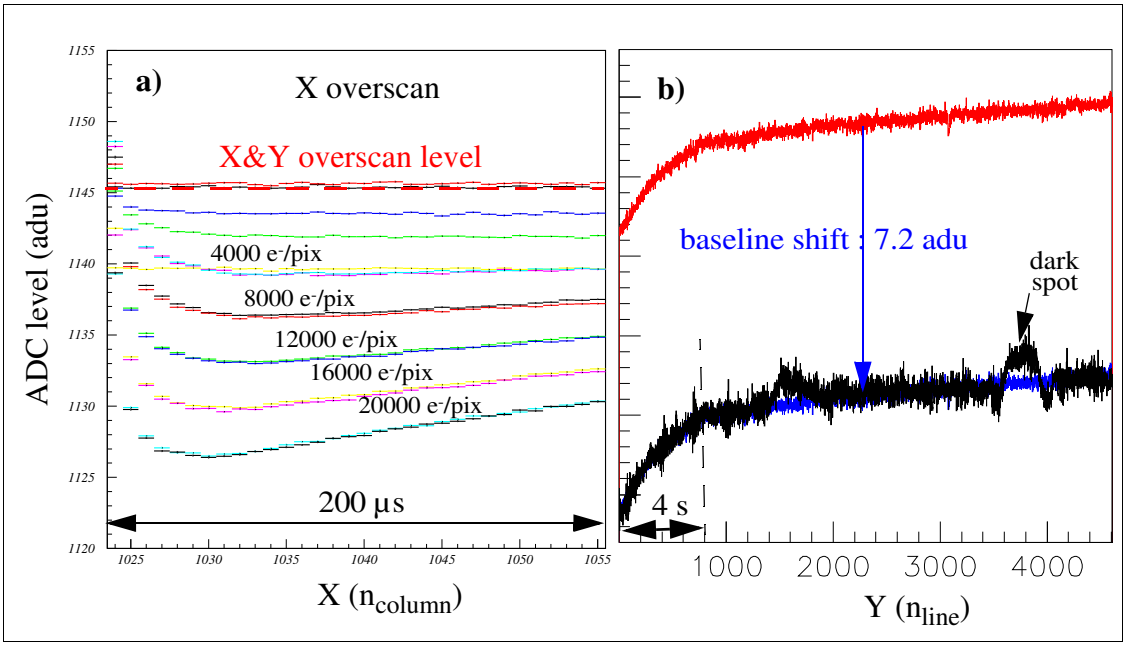

Figure 10: Stucture of the X overscan of a Megacam flat field image :
a) the X profile (Y averaged) shows the relaxation of the pedestal level following the readout of a sequence of seven uniformly bright flat field images with increasing integrated fluxes.
b) Y profile (X averaged) : in red the bias, which, when shifted by 7.2 adu (blue), compares well with the signal of the exposure at 8000 e-/pix (black). The substructures seen in the black signal correspond to trailing effect of dark spots close to the CCD edge within the image.

inside the image. It characterizes the shift of the baseline after reading a full line at high level. The time interval covered by the plot in Figure 10-a is around 200µs. The time left for a parallel line transfer, before reading the next line, is of the same order of magnitude. This is not enough to recover the rest level represented by a dashed red line just above the overscan of a low level image. The rise of pedestal level seen in Figure 10-b was already seen in the bias study and corrected. The observed phenomena are not fully explained, but some clues will be found in the study of the Megacam electronics in Appendix A.

2.5 Raw properties of the Sndice flat field exposures

The goal of this section is to obtain a first order Sndice calibration without studying in detail the diffraction rings seen in the images. The uniformity and the reproducibility of the illumination of the focal plane and the linearity[1] of the CCD response to the sndice integrated flux is supposed. (Studying the deviations from these assumptions will be the task of Section 3).

[1] the CCD transfer function which includes quantum efficiency, charge tranfer efficiency, preamplification, amplification and digitization is supposed identical for each pixel

2.5.1 Gaussian fringing

From this point of view the main characteristic of the Sndice-Megacam images is the distribution of pixel intensities gaussian with a 4% RMS except for tails above ±2σ (cf. Figure 11 a). By definition σ is the "RMS contrast" of the image. This gaussian

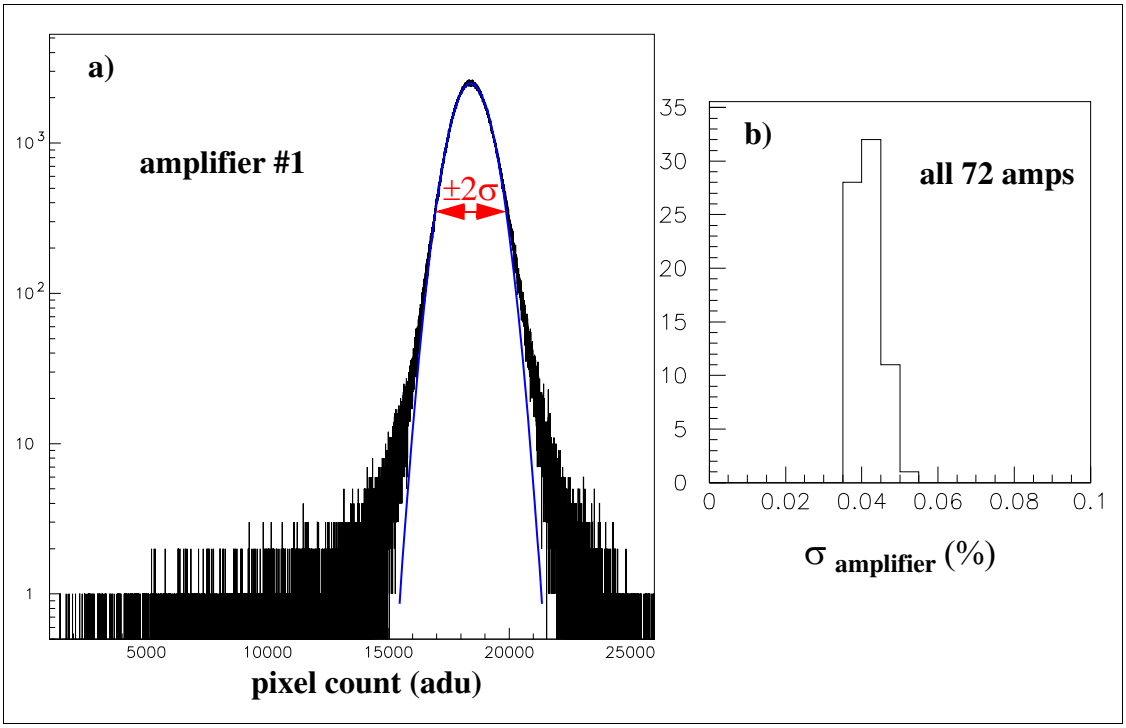

Figure 11: **a)** The single pixel ADC-count for one channel is gaussian inside a ±2σ interval (σ is by definition the RMS contrast);
b) The relative RMS contrast is rather uniformly distributed across the focal plane around 4%

dispersion is essentially due to the diffraction rings of different amplitude and scale seen in the image. It is understood as the fringing due to the interference between the specular reflection wave and the diffuse reflection waves. Therefore it is a characteristic of the roughness of the mirror surface. Let us call it "mirror fringing". It also includes the effect of the defects of the surfaces of the lens and the filters ("camera fringing"). The RMS of the photon noise ('Poisson' statistics) in a typical pixel containing $2*10^4$ e^- is 20% of the RMS contrast. Therefore it increases the RMS contrast only by 3%.
For a few channels one sees extra tails in the distribution. A dark spot on channel #21 yields an accumulation (a 'shoulder') in the dark side of the distribution as seen on Figure 12 (left). The same type of shoulder is seen in channel #24 and to a less extend in channels #16 and #20. In channel #53 and #54 there are both a dark and a bright shoulder of smaller amplitude. This is well understood by looking at the large scale image of megacam in Figure 13..The features which enter in the above description of non gaussian tails are circled. The optical defects causing the rings are often attributed to dust. We reject this hypothesis at least when the rings are aligned across the whole field (for example along the white straight line in Figure 13).
At last the distribution of channel #28, also shown in Figure 12 (right), presents a small

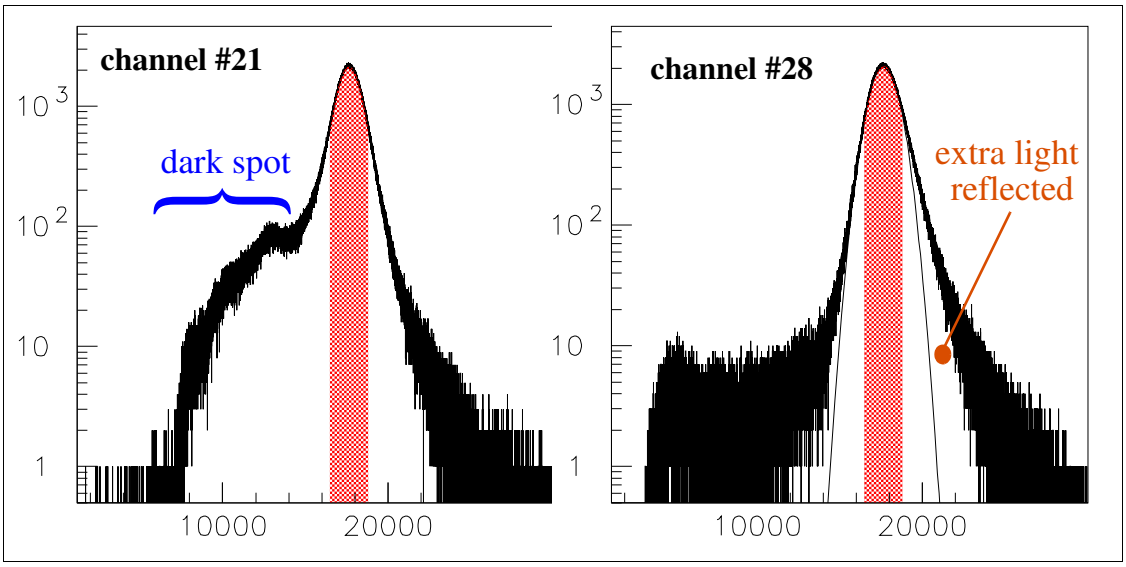

Figure 12: Compared to a normal channel in Figure 11, channels #21 and #28 present a non gaussian tail outside a ±2σ cut (in red). These features are due to defects identified in Figure 13.

bright side excess due to the glare reflecting the focal plane on the field corrector lens which yields bright filements superimposed to the normal image.

The tails can be carved out by masking problematic spots in order to yield simple gaussian distribution for all channels, or more simply by a ±2σ cut in the amplitude distribution.
The fact that the distribution of pixels measured by each channel is gaussian yields a great simplification of our analysis. The gaussian mean provides a great accuracy owing to high pixel statistics (4.8 million/channel) and yield a good calibration probe. This probe senses the product of flux, gain and quantum efficiency while ignoring the complexity of the image fine structure.

2.5.2 Global Sndice flux factor

With a flux level yielding around 35000 e/pixel, 15% of the CCD dynamical range, the statistical precision on the mean of all pixels of a channel is $2.5*10^{-6}$. This precision is limited by other factors such as gain fluctuations, but we shall reach it for other gaussian estimators which filter these fluctuations. A simple test is shown in Figure 14: Repeating a constant level illumination of megacam with sndice during one hour we obtained 25 images which were compared using the mean of all 72 channels response (around 17000 adu). The drift observed in Figure 14-a is due to the variation of sndice flux with temperature (which can be monitored either with a temperature probe at a 0.1° precision or with the photodiode inside the sndice source). A linear approximation of this temperature effect yields residuals within $1.8*10^{-4}$ RMS. This is in line with sndice known stability, but this means that the not-so-good stability of megacam electronics is not-so-bad when averaging the whole 72 channels of the focal plane.
It is known, as Corot and Kepler show for instance, that CCD cameras can reach a precision level surpassing 10^{-4}.

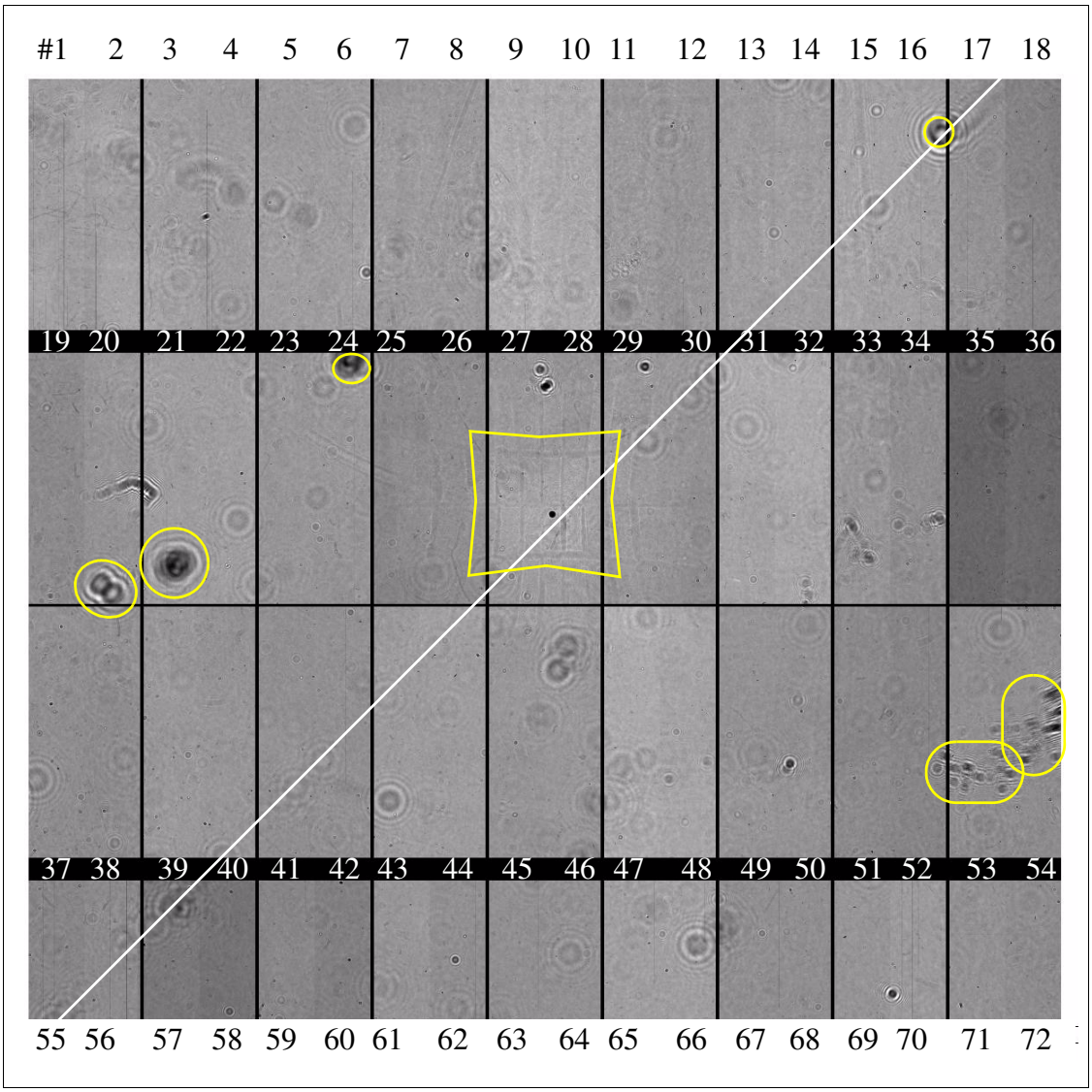

Figure 13: General view of megacam's focal plane as a mosaic of 72 channels (#1 to 72). The features yielding non-standard pixel distribution such as in Figure 12 are circled in yellow. The line traversing the field diagonnally guide the eye to follow the alignment of some optical defects

Our result indicates that our sndice light source reaches a similar level of precision. However we show in the next paragraph that individual megacam electronic channels are affected by fluctuations two order of magnitude larger.

2.5.3 Megacam image fluctuations

The distributions of pixel by pixel differences of the adc counts coming from a given electronic channel for two successive images in the 25 identical exposure sequence are represented in Figure 15. They are perfectly fitted on four order of magnitude by a gaussian representing the noise with a few outliers due to 60 hz power line noise in Figure 15-b and with cosmic rays outliers in Figure 15-a.
A non zero mean of the gaussian in Figure 15-a expresses the difference either of the gain or of the infalling flux for a given channel in two consecutive images taken at a one

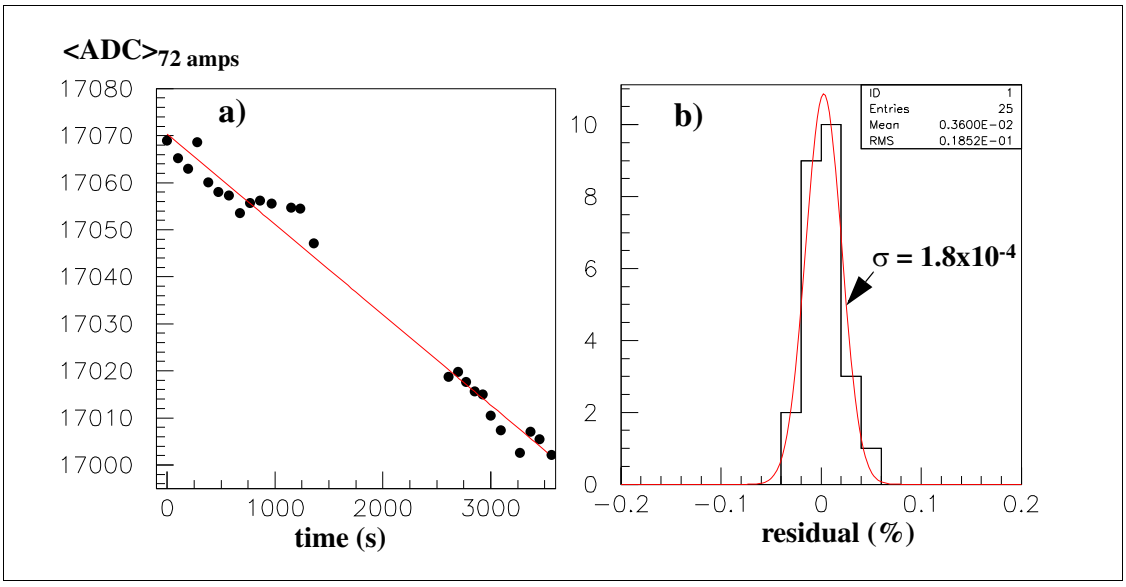

Figure 14: **a)** With 25 SNDICE light exposures taken during one hour, the average response of Megacam's 72 channels displays a small drift linear with time . **b)** A linear fit of this drift yields a residual distribution with 1.8x10^{-4} RMS attributed to the residual temperature variations.

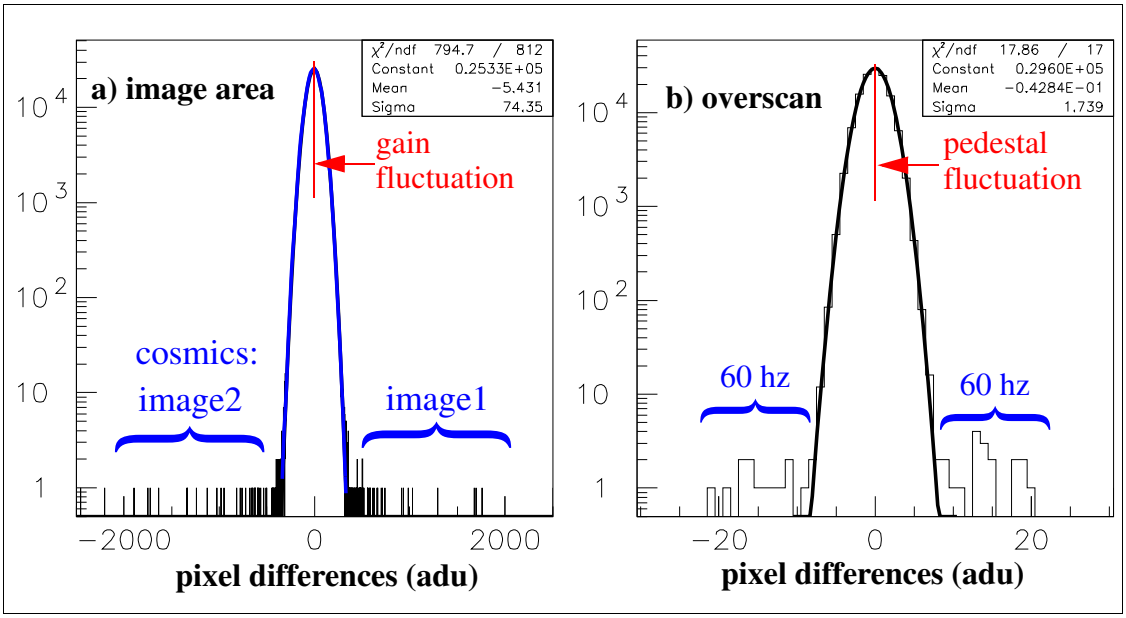

Figure 15: One channel, two consecutive images: **a)** pixel{image 1} - pixel{image 2} (cosmics outliers); **b)** same for overscan area (outliers due to 60hz power line noise)

minute interval. An overall picture of the gain×flux fluctuations of all 72 channels during one hour data taking is shown in Figure 16. It is summarized in the Figure 17 which gives in red an estimate of possible fluctuation of sndice light flux and in black the envelope of relative gain fluctuations for that exposure as a function of time.

The gaussian noise in Figure 15-b is the amplifier's Johnson noise. The gaussian noise in Figure 15-a is the Poisson noise due to electron statistics.

This Poisson noise provides an opportunity to apply a classical method which allows to determine the gain k_e of the CCD readout chain in the adu/electron unit. This method is

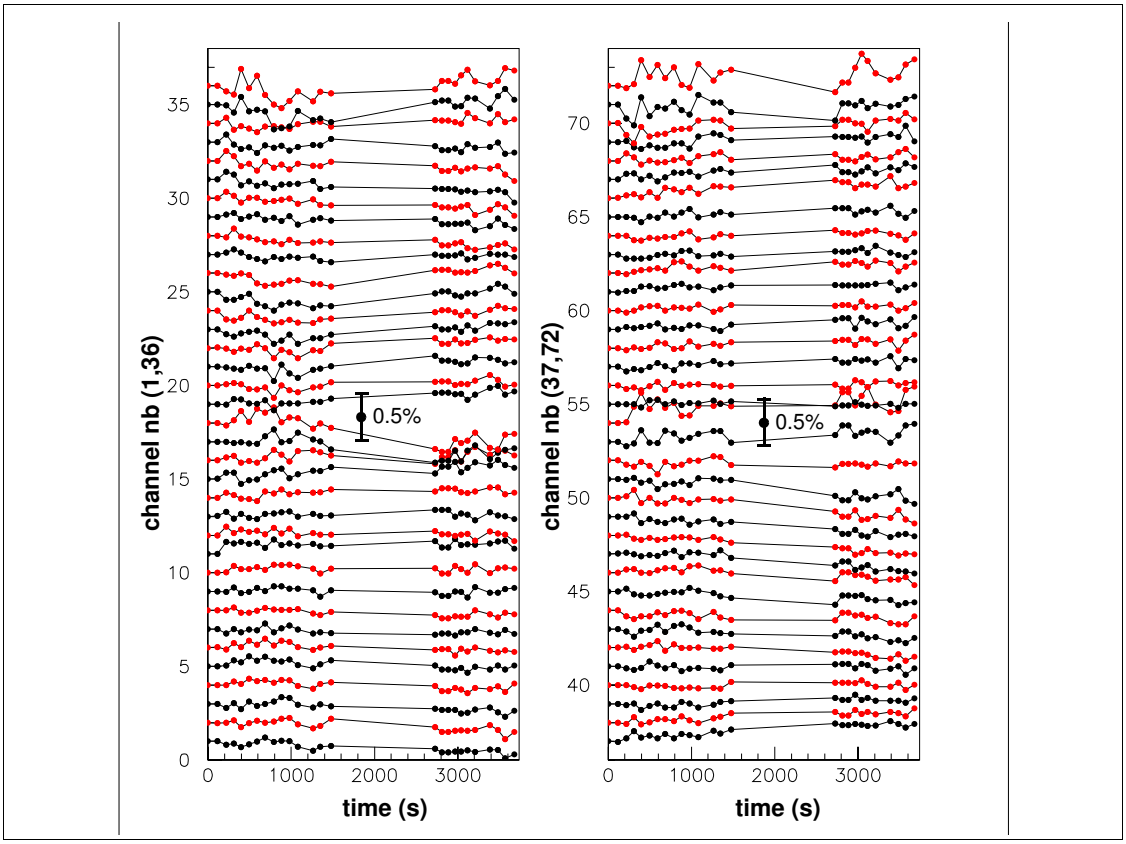

Figure 16: Fluctuation of the 72 channels gain (relative to their average) as a function of exposure time. The scale of fluctuation is given by a 0.5% bar. Statistical point to point errors due to photon statistics ($2.5*10^{-6}$) are too small to be seen.

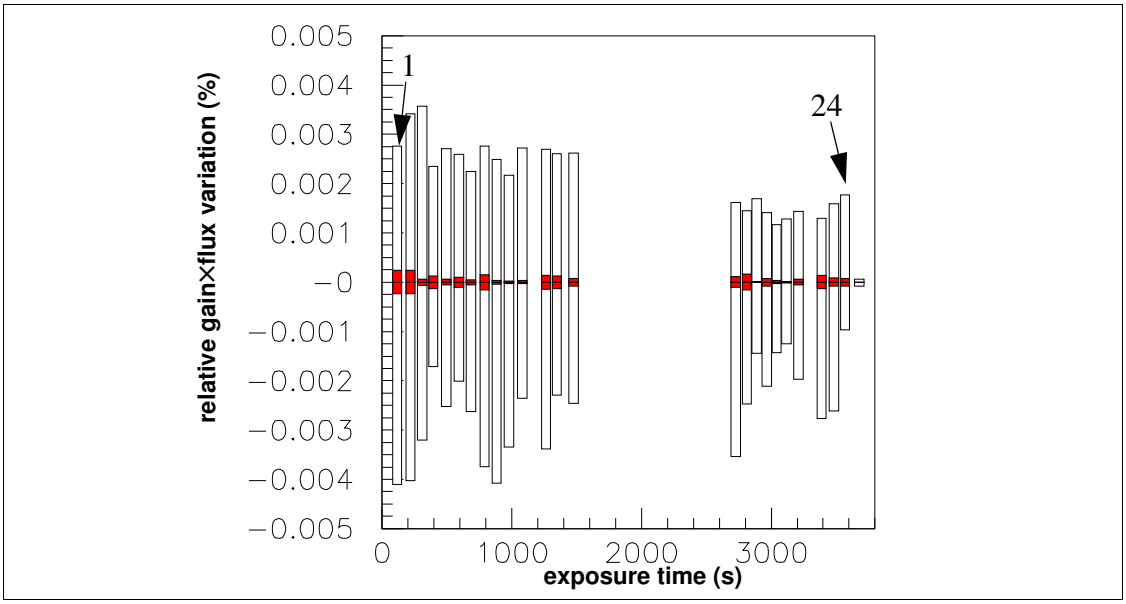

Figure 17: Black rectangles endpoints mark the extrema of the gain×flux fluctuation[a] in a channel between a current exposure (1 to 24) and the last exposure (25^{th}), as a function of the exposure time. In red an estimate of possible fluctuation of the average for all 72 channels of these fluctuations

a. relative to the average of the 72 channels

known to be delicate because of the contribution of noise sources other than Poisson. It will be refined in (??) by extracting (extra??) electronic noise (gain and pedestal fluctuations) and optical noise (fringe sliding).
Moreover we have to take into account the fact that the expected number of electron depends in a pixel varies because the "flat field" is not perfectly flat. We treat this dependence by making a regression analysis difference-versus-sum for the two charges measured in a given pixel for image-A and for image-B (cf. Figure 18-a).

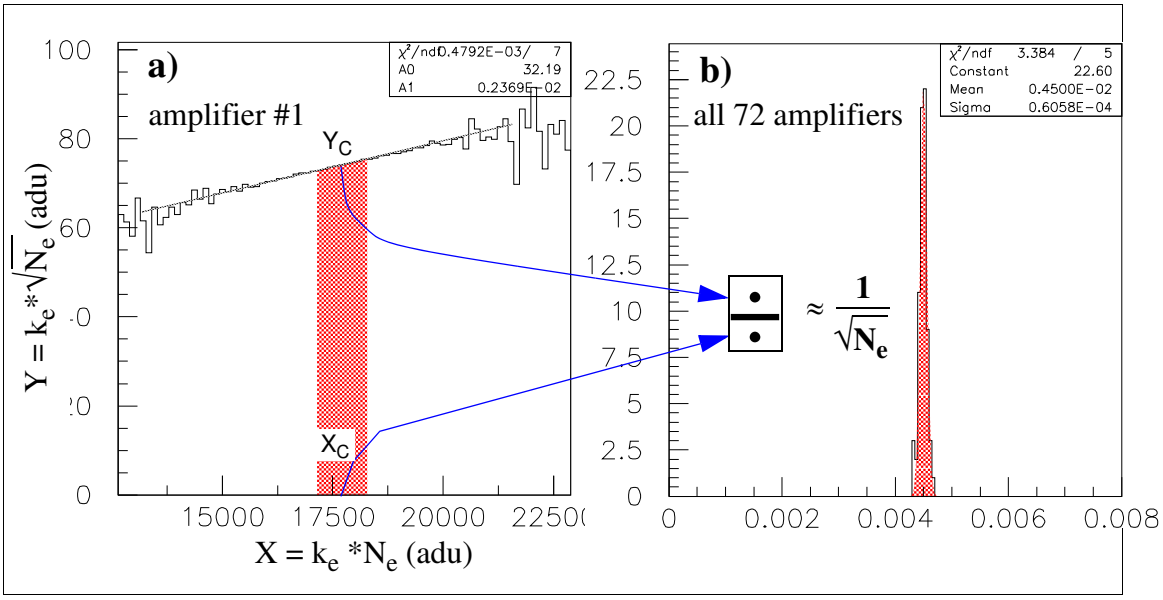

Figure 18: **a)** For each channel an X slice of image A yields Y(X)=RMS{pixel(A)-pixel(B)} and a linear fit $Y=a*(X-X_C)+Y_C$ gives a and Y_C (a equals the slope of the square root function) ;
b) : Histogram of Y_C/X_C for 72 channels (X_C is the mean of the pixel gaussian distribution).

The basic formulas for correlating the pixels of two images which follow a 2d gaussian distribution are found in Appendix C. They cover several cases: pure Poisson noise, Poisson noise added to optical "fringing noise" and uncorrelated images.
The histogram of all 72 channels in Figure 18-b displays a surprisingly small dispersion (1.5%) of the average number of electron per channel, i.e. the flux (photon/pixel) multiplied by the quantum efficiency (%) in all 72 half CCD's. This implies that both the average Sndice flux and the average QE's per channel are uniform on the 72 channels of the focal plane.
We expect to find the same quantum efficiency (QE) for both halves of a given CCD while for different CCD's, QE is dispersed due to different fabrication batches.
This fact is verified by comparing the QE difference between both halves of a given CCD to the QE difference between different CCDs. The regression analysis in Figure 19 shows that the RMS difference of the flux-times-QE measured within the two halves of a same CCD is 0.3% while the RMS dispersion of QE within the lot of 36 CCDs is 1.5%.
The quality of this measurement has been obtained by separating genuine statistical fluctuations such as Poisson noise from gain fluctuation and fringing noise. This is achieved by the Hessian filter (cf. §4.1). The reproductibility of this measurement on 72 channels for 11 images is shown in Figure 19-b to be 7×10^{-4} rms, in line with its

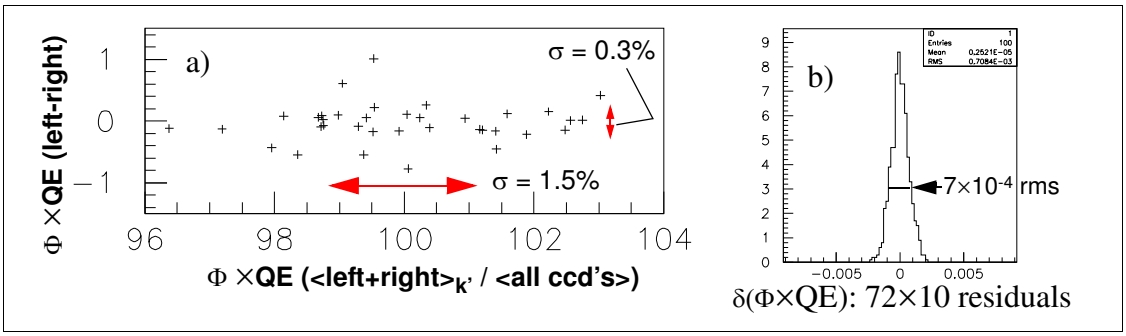

Figure 19: **a)** The difference (0.3% rms) versus the mean (1.5% rms) of the two photoelectron counts (QE ε_k weighted by the flux b_k) measured in the left and the right part of each CCD (k'=1,...,36). The QE's and the corresponding fluxes differ little. These estimators do not depend on the electronic gain. **b)** They fluctuate from an image to the next within 7×10^{-4} rms for all 72 channels and for ten images. This yields a 2.2×10^{-4} rms precision on the channel average $\phi\times$QE.

statistical value. It can be brought down by averaging. This is less sensitive than yield estimators based on the mean of all pixels in a channel (2.5×10^{-6}). But those are limited by electronic gain variation to 3×10^{-3} as illustrated in Figure 16 and Figure 17.
In addition to these variations from one exposure to the next, the example of Figure 20

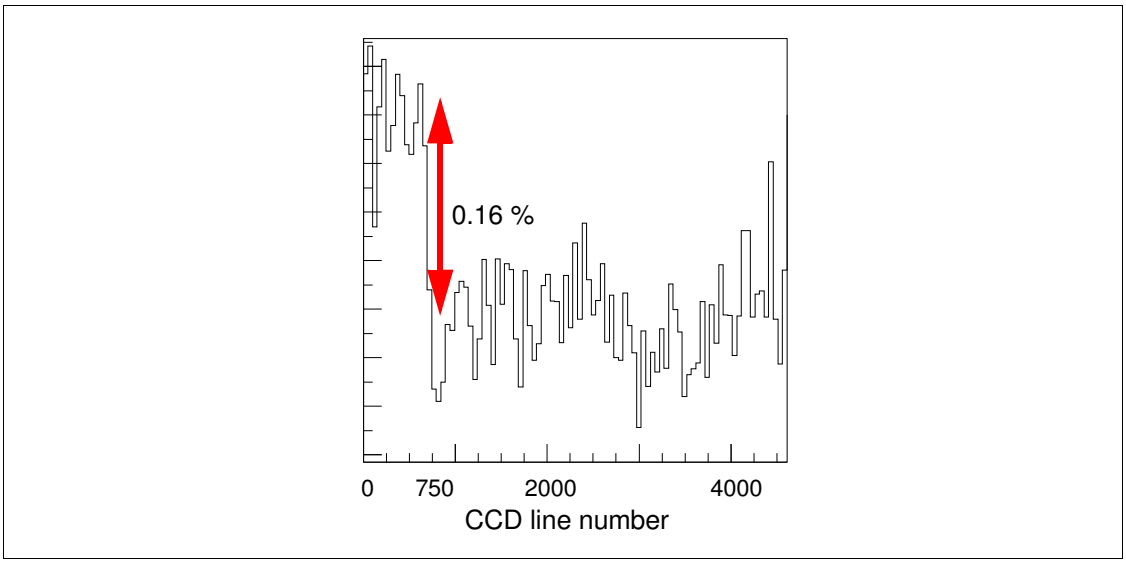

Figure 20: In this example the difference of the integrated line content for two consecutive identical CCD images as a function of the line number shows a break at line 750, understood as an abrupt 0.16% variation of the gain during the readout of the image. Fluctuations are due to fringes

shows that the electronic gain, is not really stable during one exposure. As there is no straightforward way to measure the instantaneous gain as a function of time, we shall parametrize this effect as another electronic noise. It is seen that this gain noise is essentially a low frequency noise such as pedestal noise in Figure 6-b.

2.6 Conclusion of our first order calibration study

The measurements of the Sndice light flux using megacam and the full CFH telescope are compatible with the 10^{-4} stability of the Sndice source (after temperature correction) which was established in our photometry test bench. However when trying to reach the same level of precision for the telescope calibration, the stumbling block is the lack of stability of the megacam electronics.
The best solution would be to fix the megacam electronic problems. We do not mean that it is a simple task, but it is feasible. Meanwhile we found some ways to mitigate the problem.
For the future, following a study of megacam electronics mentioned in Appendix A, we assume that modern CCD and Sndice systems would match their stability and precision performance at a better than 10^{-4} level.

We can formalize the digitization of the sndice images by megacam with an optical and an electronic transfer function linked by quantum efficiency factor, such as :

$$N^{adu}_{i,j,k,I} = \boxed{\Phi_I \times a_{i,j,k,I} \times b_k} \times \varepsilon_{k'} \times \boxed{g_{k,I} + \wp_{i,j,k,I}} \qquad \begin{matrix} \Phi_I = \phi_I \times \Delta t \times L(I) \\ \sum_{i,j} a_{i,j,k,I} = 1 \\ \wp_{i,j,k,I} \leftrightarrow equ(1) \end{matrix} \qquad (2)$$

optical — electronic — opto-electronic

$N_{i,j,k,I} = \Phi_I \times a_{i,j,k,I} \times b_k \times \varepsilon_{k'} \times g^2_{k,I}$ is the expected content of a given pixel i,j,k for image I (in ADC unit) and $\delta^2 N_{i,j,k,I}$ its variance,
Φ_I is the integrated LED light flux for image I which is proportional to the exposure time Δt and linearly dependent on temperature T and the LED current,
$a_{i,j,k,I}$ is the conditional probability for a photon to fall in a given pixel i,j if it falls on the half CCD read by channel k during the exposure I,
b_k is the fraction of total photon flux falling on channel k,
$\varepsilon_{k'}$ is the quantum efficiency of the CCD k',
$g_{k,I}$ is the electronic gain of channel k in image I and $\delta g_{k,I}$ the RMS of its fluctuations,
$\wp_{i,j,k,I}$ is the pedestal, a sum of three components and their noise.

Assuming that the system is fully calibrated, the optical part is expressed in photon number $n_{i,j,k,I}$ with a poisson statistical fluctuation $\delta n_{i,j,k,I}$.
The determination of the pedestals $\wp_{i,j,k,I}$ is based on bias frames parametrization of 1. Some runs are rejected, when large deviations (up to 40 adu) from a six month average is established. The remaining pedestal residuals $\delta\wp_{i,j,k,I}$ are smaller than 1 adu and add up to the 2 adu electronic white noise.
The rest of the transfer function is determined relatively to a reference image I_{ref} with a reference flux Φ_{ref} and a reference channel k_{ref} .
Two continuity hypotheses are used to connect the reference channel in the reference image to all channels in one image and to all images in a sequence : the continuity of the optical flux in each image and the stability of the average of the 72 channels gain during a sequence of images. Consequently we shall be able to test a third hypothesis, the stability of the images $a_{i,j,k,I}$ of the sequence $I_{min}<I<I_{max}$.

We call “stitching” the process of connecting the data of all channels in one image to the data of the reference channel by adjusting the coefficients b_k ($1<k<72$) in order to minimize the discrepancy across the channel boundaries. The stitching of the left half with the right half of a given CCD is assured within the 10^{-4} error due to photon statistics. The stitching of all 36 CCDs is more delicate due to gaps in between CCDs but almost as precise in practice. The tracking of the fluctuations for each channel $b_k \times \varepsilon_{k'} \times g_{k,I}$ relative to the average $G_I = \langle b_k \times \varepsilon_{k'} \times g_{k,I} \rangle_k$ has been shown in §2.5.3. In this paragraph Figure 16 has shown that the relative gain of certain channels $g_{k,I}/G_I$ can vary as much as a half percent from one image to the next.
By assuming that the CCD quantum efficiencies $\varepsilon_{k'}$, the fraction of flux impinging upon CCDs b_k and G_I are constant during a sequence of images all gains are then aligned and the instabilities of the electronic part of the transfer function have been mitigated. This gives all the parameters of 2 in ADC units and relative to the reference aforementioned with a 10^{-4} error. The last two steps to have an absolute calibration of the focal plane in number of photon units would be :

1) to have a statistical analysis such as in Figure 19 measuring the electron/adu ratio.
2) to have an absolute calibration of the reference CCD such as the CLAP calibration.

We have established that the electronic response vary also during the readout of an image for example in Figure 19 b). We consider this fluctuation as a gain noise $\delta g_{k,I}$ to be added to the Poisson noise. Therefore this gain noise affects the measure of the electron/adu ratio based on the Poisson noise, but we do not know yet how to suppress it. Similarly the fringes in the images move haphazardly yielding a fringe noise which can double the Poisson noise. It is represented by a unitary transformation $a_{i,j,k,I} \rightarrow a_{i,j,k,I} + \delta a_{i,j,k,I}$ studied in §4.3.
Moreover our parametrization in 2 has been proved only for very small variation of flux due to variation of LED temperature. We must prove that it holds for the large variations constituting a “level ramp”. Level ramps are necessary to check the linearity of the model and to give clues identifying noise sources.

3 Adapting calibration paradigm and methodology to SNDICE fields

In the preceding conclusion we fixed two goals which needed some technical developments : differentiation of noise sources other than Poisson statistics and processing of level ramp images.
For that reason we develop in this section a new methodology adapted to the two main optical characteristics of the Sndice fields impinging upon the megacam focal plane inside the CFH telescope :

1. Precision and stability better or equal to 10^{-4}.
2. Fringing with a gaussian amplitude spectrum.

Obviously we cannot base our method on a simple photometric paradigm akin ray optics. We need to follow wavefronts issued from the LED cristal through the telescope to the

focal plane where the wavefunction collapses. Fringes in our images are visible due to the small angular diameter of the LED seen at a f=15m distance. They contain an enormous microscopic information on the real transfer function of the optical surfaces, mirror and camera, beyond a simple geometrical definition. A common approach consisting in extending the size of the source[2] to suppress the fringes and make the analysis simpler amounts to sweep details under the rug. We would rather do the contrary : increase fringe visibility because fringes are an unique probe for the true transfer function of a telescope. For computing the transmission efficiency through lens and filters think to the difference between absorptive and optical cross section of defects. For computing the mirror reflection efficiency remember that diffuse reflection is not contained in the psf while specular reflection is. A common objection is based on the simplicity of "incoherent" flat fields and the convenience of telescope geometrical optics models. Our answer is to develop in this paper simple algorithms working on gaussian fringed fields and in a later paper to develop a simplified geometrical model representing only the transmitted specular wave.

Before embarking in this study, we should recall that the CCD focal plane should have been tested initially with the Sndice source alone at f=15m distance. Without mirror fringing this would make the CCD response to the LED wavefront flat and its analysis, including some eventual CCD fringing[3], rather straightforward.

3.1 Aspect of the fringes found in Sndice-Megacam images

As seen earlier in Figure 11 the RMS contrast in the surface covered by one CCD channel is σ~4% and rather uniform. In order to visualize how the fringes yield this contrast we put in Figure 21 an image of the quarter of a CCD channel using a black-to-white grey scale covering the interval [-1.5 σ ,+1.5 σ] around the average level. A closer look shows that in 'normal' areas D and E the effect of darker and brighter rings are averaged out by projection leaving a low X frequency variation and a high X frequency noise both of the order of one per mil. In B and E we see that the effect of dark rings is visible in projection as a 1.5% dip. The projection act as a low pass filter in one dimension which reduces the 4% diffractive noise to less than a percent. But it reveals also non diffractive absorbing effects such as the deep (3%) dark spot in the upper left of A, or a shallower one in C. Sharper and smaller rings due to camera defects are scattered everywhere. Three of them in the D area are pointed and circled in blue.

3.2 Fluctuations of Megacam images

When comparing sndice-megacam images taken at one minute intervals we find a rather paradoxical situation. First the pixel distribution is essentially gaussian as predicted for perfectly reproducible images with 0.7% Poisson noise seen in Figure 15-a, but if we subtract the two images and visualize the result, as we do in Figure 22,, we discover

---

[2] simply by putting a diffuser in front of the LED

[3] CCD fringing is reduced by the relatively large LED spectrum

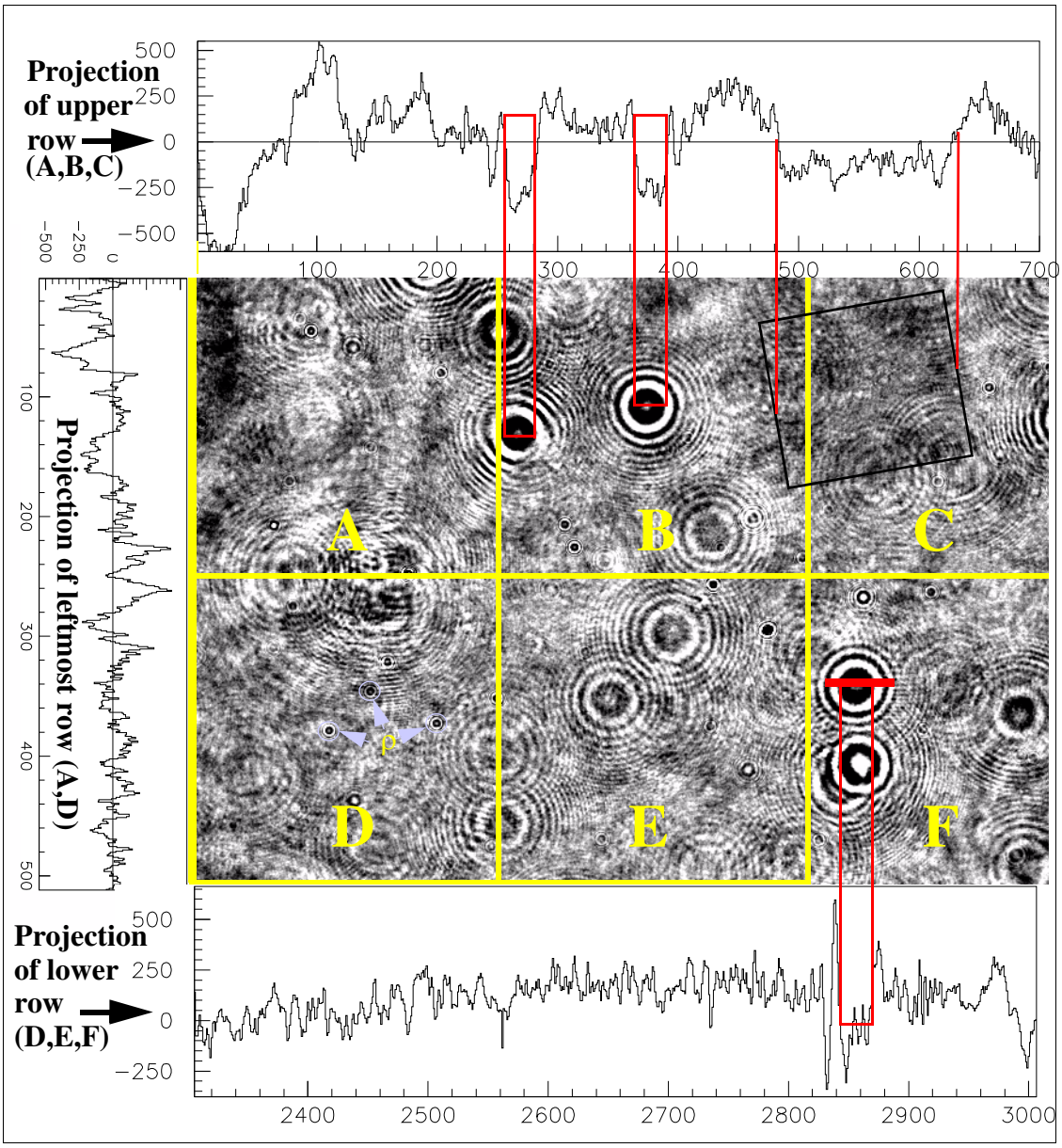

Figure 21: The underlying megacam image is drawn pixel by pixel with a grey scale around the average level (black=<-5%; white >+5%). Six 'Superpixels' (512*512 pixels) are labeled A to F. The projection of A-B-C and D-E-F rows on X axis are seen on top and bottom sides and the A-D projection on Y is seen on left side. The three dark round spots in B and F are projected on the sides by red rectangles. A rectangular grey area in C is also projected on top side. Three small rings in D are circled and pointed in blue (marked as ρ).

many patterns which give a signature for different sources of non reproducibility either from megacam electronics or from optical transmission effects.

This situation will be understood quantatively in the following sections after the introduction of filters which are specifically sensitive to the different sources of non reproductivity. Qualitatively when looking at Figure 22 we filter the underlying structures involving many pixels by using mental image processing.

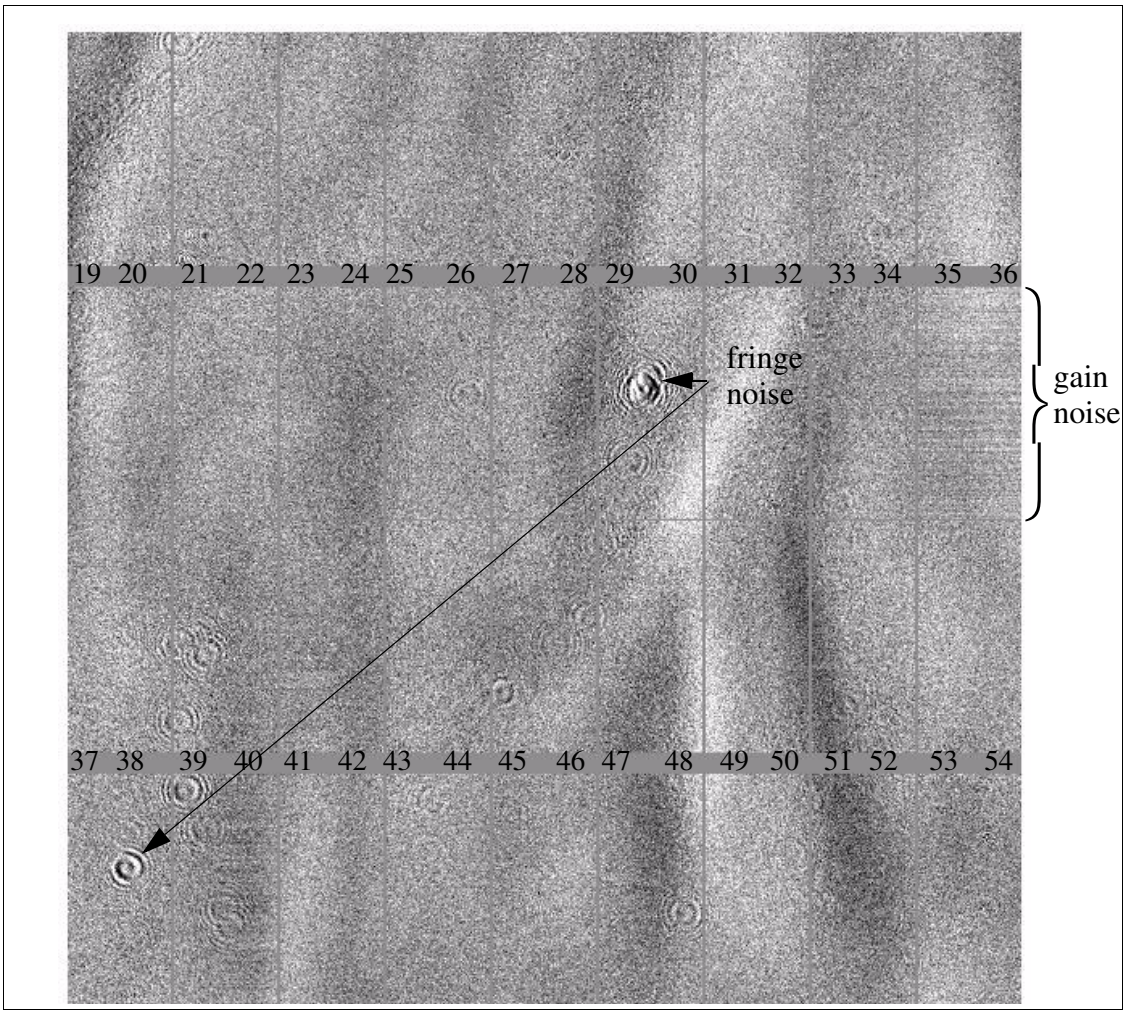

Figure 22: This differential Megacam image is made by a pixel to pixel subtraction of two consecutive images obtained with identical SNDICE illumination followed by summing 16x16 pixel areas. Grey scale is between ±1%. The same low frequency gain noise is seen on two neighbour channels #35 and #36. Fringe noise due to a shift of the fringe pattern between the two exposures yields a differential fringe pattern. The cause of the overall shade pattern is not clearly identified.

a) Electronic gain variations are best shown in Figure 22 by horizontal strips on channels 35 and 36. In the same channels pedestals are affected by a similar effect attributed in Figure 6 to microphonics.

b) Displacement of fringes on CCDs, which is measured as shown in Figure 25 with a 0.3µ precision, causes the main optical instability. It yields the ring structures clearly seen in Figure 22.

c) Large scale shades overlying channel boundaries are not yet identified.

4 Gaussian model of Sndice-Megacam images

We have established as a conclusion of our first chapter in §2.6 a formula relating the adc measurement of each pixel $N_{i,j,k,I}$ to an expected photon number $a_{i,j,k,I}$. The principal

information on the fringed field so far is the quasi-gaussian distribution of $a_{i,j,k,I}$ and the perfectly gaussian distribution of $a_{i,j,k,I+1} - a_{i,j,k,I}$ for a given channel k in the image I. We will introduce differential operators which will help us to constrain the description of the fringe images by continuity arguments. One can find a review on the mathematical uses and the image analysis uses of such operators in the context of Image Analysis [5] where they are called "Partial Differential Equations" (PDE). What makes these operators even more useful is that they distinguish between the random Poisson fluctuations and the highly correlated electronic and optical fluctuations. Moreover they yield a lossless compression of digital image data.

4.1 Mathematical introduction of the four operator basis α, β, γ, δ

We introduce in 3 four operators α, β, γ, δ acting independently on each "quartet" (a 2×2 matrix of adjacent pixels):

$$\left[a_{i,j}\right]_{k,I} \leftrightarrow \left[\alpha_{i_1,j_1}\right]_{k,I} \cup \left[\beta_{i_1,j_1}\right]_{k,I} \cup \left[\gamma_{i_1,j_1}\right]_{k,I} \cup \left[\delta_{i_1,j_1}\right]_{k,I}$$

$$\begin{aligned}
\alpha_{i_1,j_1} &= (a_{2i_1-1,\,2j_1} + a_{2i_1,\,2j_1} + a_{2i_1-1,\,2j_1-1} + a_{2i_1,\,2j_1-1})/2 \qquad i = 1,1024 \\
\beta_{i_1,j_1} &= (a_{2i_1-1,\,2j_1} + a_{2i_1,\,2j_1} - a_{2i_1-1,\,2j_1-1} - a_{2i_1,\,2j_1-1})/2 \qquad j = 1,4610 \\
\gamma_{i_1,j_1} &= (-a_{2i_1-1,\,2j_1} + a_{2i_1,\,2j_1} - a_{2i_1-1,\,2j_1-1} + a_{2i_1,\,2j_1-1})/2 \qquad i_1 = 1,512 \\
\delta_{i_1,j_1} &= (-a_{2i_1-1,\,2j_1} + a_{2i_1,\,2j_1} + a_{2i_1-1,\,2j_1-1} - a_{2i_1,\,2j_1-1})/2 \qquad j_1 = 1,2305
\end{aligned} \tag{3}$$

They have simple algebraic properties reflecting our simple reasons to build them.
Notably the 4×4 matrix transforming the four adjacent pixels into the vector (α, β, γ, δ) is orthogonal. What we have written in 3 is a much larger matrix 1024×4610 made of 512×2305 such 4×4 blocks. A more physical way to consider this mathematical operation is that we apply to the original 1024×4610 image successively four spatial frequency halving operators which yield four different 512×2305 images named α, β, γ and δ .
Let us write down how these operators can be built from simpler two pixel operators:
$\Sigma_x : (a_{i,j}\,,\, a_{i+1,j}) \rightarrow (a_{i,j} + a_{i+1,j})/\sqrt{2}$; $\quad \Delta_x : (a_{i,j}\,,\, a_{i+1,j}) \rightarrow (a_{i+1,j} - a_{i,j})/\sqrt{2}$
$\Sigma_y : (a_{i,j}\,,\, a_{i,j+1}) \rightarrow (a_{i,j} + a_{i,j+1})/\sqrt{2}$; $\quad \Delta_y : (a_{i,j}\,,\, a_{i,j+1}) \rightarrow (a_{i,j+1} - a_{i,j})/\sqrt{2}$
Practically the differential operators Δ are part of a (Σ, Δ) doublet which creates a reversible operation yielding two images while halving the number of lines (or columns). In order to conserve an x×y symmetry we use the product $(\Sigma, \Delta)_x \times (\Sigma, \Delta)_y$. Each image yields four images with half the number of lines and half the number of columns, namely: $\Sigma_x\times\Sigma_y$; $\Sigma_x\times\Delta_y$; $\Sigma_y\times\Delta_x$; $\Delta_x\times\Delta_y$ that we can identify respectively with α, β, γ and δ :
$\alpha = \Sigma_x\times\Sigma_y$ the mean of the quartet
$\gamma = \Sigma_y\times\Delta_x$ and $\beta = \Sigma_x\times\Delta_y$ are the x and y components of the gradient of the image
$\delta = \Delta_x\times\Delta_y$ is the non-diagonal component of the Hessian matrix of the image

Alternatively one can choose a basis aligned on the diagonal vector u and v instead of x and y. This formalism is even simpler for image processing as shown in [4].

$\Sigma_u : (a_{i,j}\ ,\ a_{i+1,j+1}) \rightarrow (a_{i,j} + a_{i+1,j+1})/\sqrt{2}$; $\quad \Delta_u : (a_{i,j}\ ,\ a_{i+1,j+1}) \rightarrow (a_{i+1,j+1} - a_{i,j})/\sqrt{2}$

$\Sigma_v : (a_{i+1,j}\ ,\ a_{i,j+1}) \rightarrow (a_{i+1,j} + a_{i,j+1})/\sqrt{2}$; $\quad \Delta_v : (a_{i+1,j}\ ,\ a_{i,j+1}) \rightarrow (a_{i,j+1} - a_{i+1,j})/\sqrt{2}$

Δ_u and Δ_u provide an orthonormal basis for the gradient. A $\pi/2$ rotation matrix relate this base to the β and γ base.

4.2 Statistical properties of the distributions of our four operators applied to one image

The image generated by operator α (a sum of four neighbour pixels) has almost the same distribution as the raw pixel image but for a lower x and y resolution and a lower noise. The operators β and γ yield a couple of "partial differential images" representing the gradient field. The operator γ is imaging the non diagonal term of the Hessian matrix. We have studied these four images empirically because there is no model to describe the field generated mainly by the defects of the telescope optical surfaces. Pushing further the processing of these four digital images permits to resolve individual fringes (cf. ref. [4]) but not to calibrate the transfer function of the telescope. We leave that to future studies. Fortunately the statistical properties of the images of the four operators are mathematically simple and constrained by global symmetry arguments:

1. The 4-d probability distribution of α, β, γ, δ is gaussian
2. The distributions of β and γ are absolutely identical, perfectly centered and left-right symmetric (cf. ref. [2]§7.3.2). This is easily understood because there is no privileged orientation of the gradient. The distribution of α is centered by subtracting the fitted center $<\alpha>$ of the gaussian. It becomes $\alpha' = \alpha - <\alpha>$.
3. The gaussian width of β and γ is a quarter of α's. They are gaussian inside a $\pm 2\sigma$ cut and have a 1% non gaussian tail outside $\pm 2.5\sigma$ essentially due to the sharp rings of camera fringing (marked ρ in Figure 21). The distribution of δ is a gaussian with a gaussian width a sixth of α's.
4. We apply a gaussianity test on the joint distributions of all couples of operators by the conditional probability method of Appendix C. First the method checks the gaussianity of each slice of the 2-d distribution and then it parametrizes the curves described by the means and the rms as a function of the slice variable. The mean curve is usually identically null or otherwise described by a straight line (or a parabola) whatever the slice is. For the (α,β), (α,γ) and (α,δ) couples the RMS is rising with the amplitude of α owing to the $\sqrt{\alpha}$ dependence of the Poisson noise. This is the main deviation from a gaussian law.

Let us write down these properties and give an approximate value at mid ADC range :

$$\alpha' = \alpha - \langle\alpha\rangle \qquad \langle\alpha'\rangle = \langle\delta\rangle = \langle\beta\rangle = \langle\gamma\rangle = 0 \qquad \sigma_{\beta_{I_1}} = \sigma_{\gamma_{I_1}}$$

$$at \sim 300000 \quad e/pix$$

$$\sigma_{\alpha_{I_1}} \approx 3.5\% \times \alpha_{I_1} \qquad \sigma_{\beta_{I_1}} = \sigma_{\gamma_{I_1}} \approx 0.9\% \times \alpha_{I_1} \qquad \sigma_{\beta_{I_1}} \approx 0.6\% \times \alpha_{I_1}$$

For each image I there are 72 symmetric 4×4 matrices $C_{I,k}$, one per electronic channel k :

$$C_{I_1,k} = \begin{bmatrix} \sigma^2_{\alpha' I_1} & \langle\alpha'_{I_1}|\beta_{I_1}\rangle & \langle\alpha'_{I_1}|\gamma_{I_1}\rangle & \langle\alpha'_{I_1}|\delta_{I_1}\rangle \\ & \sigma^2_{\beta I_1} & \langle\beta_{I_1}|\gamma_{I_1}\rangle & \langle\beta_{I_1}|\delta_{I_1}\rangle \\ & & \sigma^2_{\gamma I_1} & \langle\gamma_{I_1}|\delta_{I_1}\rangle \\ & & & \sigma^2_{\delta I_1} \end{bmatrix}_k = \begin{bmatrix} \sigma^2_{\alpha k, I_1} & 0 & 0 & 0 \\ 0 & \sigma^2_{\beta k, I_1} & 0 & 0 \\ 0 & 0 & \sigma^2_{\beta k, I_1} & 0 \\ 0 & 0 & 0 & \sigma^2_{\delta k, I_1} \end{bmatrix} \quad (4)$$

The nullity of non-diagonal covariance terms is a great asset of the representation on the (α, β, γ, δ) base. It means that we can use the four quantities globally (1024×1024 pixel scale) as if they were independent variables, although they are not independent on a local scale (say 25×25 pixels).

When we replace in 3 the pixel probability $a_{i,j,k,I}$ by the expected adu count $N_{i,j,k,I}$ taken from 2 and then compute the covariance matrix, we get the matrix of 4 multiplied by a common factor $(\Psi_{k,I})^2$. The parameter $\Psi_{k,I}=\Phi_I \times b_k \times \varepsilon_k \times g_{k,I}$ is the factor flux×efficiency×gain already computed from raw pixel sums in Section 2.6. It gave us, when averaged over the 72 channels, an estimation of the total flux in the image at a 10^{-4} precision.

The four independent RMS measurements appearing in 4 contain the factor $\langle\Psi_{k,I}\rangle_k$, one for each operator. They are in good agreement with the general flux estimator shown in Figure 23. Noise variations contributes to the discrepancy in proportion with the

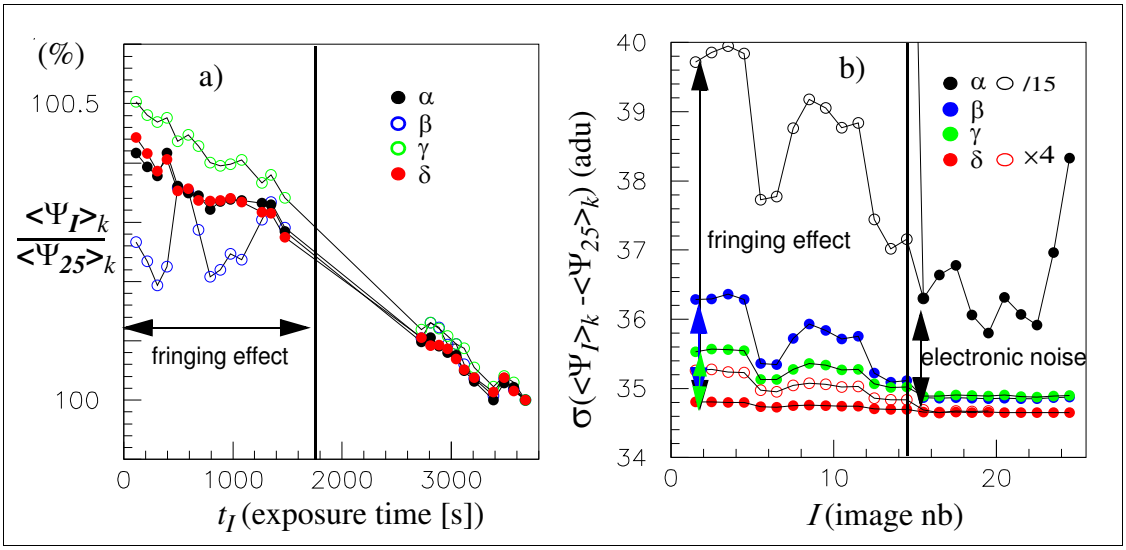

Figure 23: **a)** Relative flux estimators $\langle\Psi_{k,I}\rangle_k / \langle\Psi_{k,25}\rangle_k$ for α, β, γ, δ operators from image 1 to 25 **b)** Root mean square deviations between images *I*=1,24 and I=25 (averaging all 72 channels). The scale of fluctuations of the 14 first images relative to the last one are amplified by a factor 4 for filter δ and reduced by a factor 15 for α in order to be seen.

absolute value of the signal. One remarks that the noise is larger for the vertical gradient

(γ) than for the horizontal one (β). Particularly the δ estimator which is in a 10^{-4} agreement with α, shows an insensivity to all sources of noise down to the 0.3×10^{-6} statistical error.
In order to understand quantitatively the effect of the noise one has to use the detailed model of gaussian variables developped in Appendix C. It is based on the fact that adding two gaussian variables yield a new gaussian variable which covariance matrix is the sum of both their covariance matrices.
The reference signal <α>, which is the average of four adjacent pixels, is about 17000 adu.

filter	α	α'	β	γ	δ	**Comments**
< **filter** > (adu/pix)	17000	≤0.1	≤0.1	≤0.1	≤0.1	cf.Figure 24b
σ_{fringe} /<α> %	3.5	3.5	0.9	0.9	0.6	
$\sigma_{poisson}$ /<α> %	$0.35\sqrt{\alpha_0/\alpha}$	$0.35\sqrt{\alpha_0/\alpha}$	$0.35\sqrt{\alpha_0/\alpha}$	$0.35\sqrt{\alpha_0/\alpha}$	$0.35\sqrt{\alpha_0/\alpha}$	$\alpha_0\leftrightarrow$17000 adu
$\delta_{\wp}$ ($e^-\approx$<α>/30000)	4	4	4	4	4	el. noise eq.(1)
δg /<α> %		0.1	0.027	0.027	<0.0001	gain noise
$\delta a_{i,j,k,l}$ /<α> %		0.01-0.35			<0.0001	fringe noise

Table 1: Order of magnitude of the various signals and noises contributing to the Sndice/Megacam images

The averages of the four other operators are null, as found on first line of table 1. The effect of the noise components on the relative flux estimators and the global noise estimators are seen on Figure 23 a) and b) respectively. A vertical bar separates the first 14 images where fringing differs significantly from image 25. For the last 10 images δ filter noise is only due to Poisson, while the small enhancement of the noises in the β and γ filter and the larger one in the α filter is due to the electronic noise. These data are translated into the numbers figuring in the table 1 to fix an order of magnitude for the parameters of our image model.

4.3 Statistical comparison of two images in a sequence

The simplest comparison of two images is a subtraction as in Figure 15 or in Figure 22. To make it more rigorous we shall translate this operation in the gaussian variable framework of the previous paragraph.
For more compact formulas we introduce the quadrivector $\Xi_{I,k}=(\alpha', \beta, \gamma, \delta)_{I,k}$. A one image formalism needs the 4×4 covariance matrix in 4 is $C_{I,k}=cov(\Xi_{I,k}, \Xi_{I,k})$. A two image formalism introduce an eight-vector $(\Xi_{I,k}, \Xi_{2,k})$ and its 8×8 covariance matrix expressed as a 2×2 block structure:

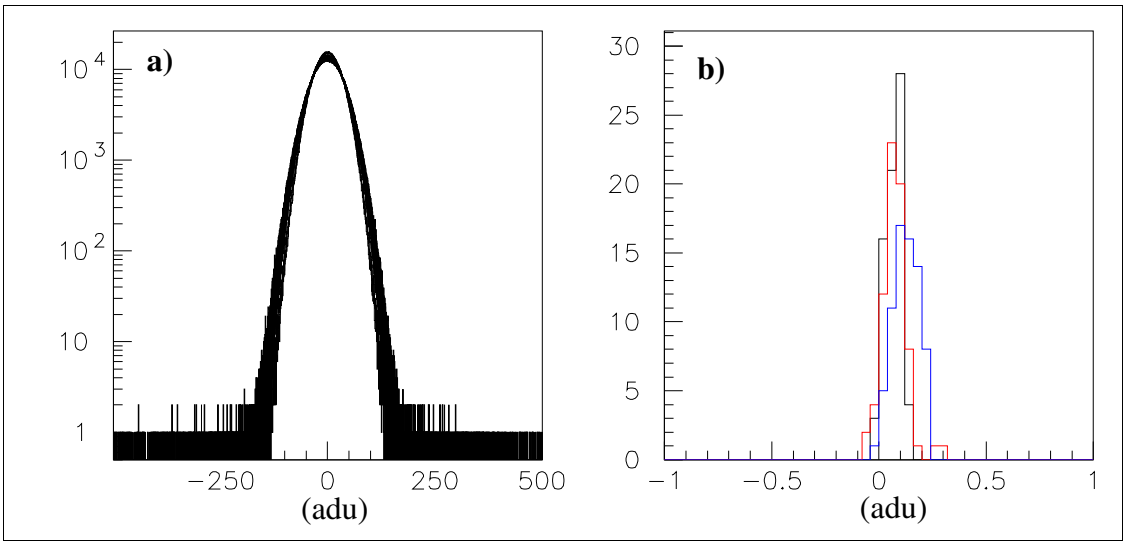

Figure 24: **a)** Gaussian test : The distributions of the difference of pixel contents between two consecutive «$\Delta_x \times \Delta_y$ images» (72 gaussians are overdrawn -one per channel).
b) Nullity test : in black the distribution of mean values of the 72 $\Delta_x \times \Delta_y$ gaussians (blue and red : the same for $\Delta_x \times \Sigma_y$ and $\Sigma_x \times \Delta_y$)

$$C_{(I_1 \oplus I_2),k} = \left\langle \begin{bmatrix} \Xi_1 \\ \Xi_2 \end{bmatrix} \times \begin{bmatrix} \Xi_1 & \Xi_2 \end{bmatrix} \right\rangle = \begin{bmatrix} [C_{I_1,k}] & [C_{I_{1\otimes 2},k}] \\ [C_{I_{1\otimes 2},k}] & [C_{I_2,k}] \end{bmatrix} = \begin{bmatrix} [C_{I_1}] & [C_{I_{1\otimes 2}}] \\ [C_{I_{1\otimes 2}}] & [C_{I_2}] \end{bmatrix}_k \quad (5)$$

The two diagonal blocks are diagonal themselves as shown in 4. The antidiagonal block, appearing twice because of the symmetry of the overall matrix, is equal to both diagonal blocks if both images are identical.

4.3.1 Effect of fringe shifting on a sequence of images with constant flux

If two images are different due to fringe shifting, non diagonal terms η_x and η_y appear correlating α' and respectively β and γ. They measure a shift of the fringes contained in the area of channel k respectively in the x and y directions. To understand intuitively this effect one has to go back to the deep reason of the nullity of the two terms which correlate the amplitude and its derivatives in x and y. The amplitude as a function of x (or y) oscillate. Its first derivatives oscillate in quadrature and its second derivatives in opposition of phase. For a given image and for one amplitude value f(x)=A there are many pixels $x_1,...,x_n$ with $f(x_1)=...=f(x_n)=A$ with alternatively positive and negative derivatives $f'(x_1),...,f'(x_n)$.
Their sum average to zero: $f'(x_1)+...+f'(x_n)=0$. When correlating image I_1 f(x) with image I_2 f(x+Δx) the derivative correlated to the amplitude f(x) is no more f'(x) but $f'(x+\Delta x)= f'(x)+f''(x)\Delta x$. The global sum of $f'(x_1+\Delta x)+...+f'(x_n+\Delta x)$ is equal to $[f'(x_1)+...+f'(x_n)] + [f''(x_1)+...+f''(x_n)]\Delta x$. The first bracket in the sum is null and the second is of a constant sign opposite to $f(x)\Delta x$.

$$C_{I_{1\otimes 2},k} = \begin{bmatrix} \langle \alpha'_{I_1} | \alpha'_{I_2} \rangle & \langle \alpha'_{I_1} | \beta_{I_2} \rangle & \langle \alpha'_{I_1} | \gamma_{I_2} \rangle & \langle \alpha'_{I_1} | \delta_{I_2} \rangle \\ & \langle \beta_{I_1} | \beta_{I_2} \rangle & \langle \beta_{I_1} | \gamma_{I_2} \rangle & \langle \beta_{I_1} | \delta_{I_2} \rangle \\ & & \langle \gamma_{I_1} | \gamma_{I_2} \rangle & \langle \gamma_{I_1} | \delta_{I_2} \rangle \\ & & & \langle \delta_{I_1} | \delta_{I_2} \rangle \end{bmatrix}_k = \begin{bmatrix} \sigma^2_{\alpha'_{I_{1\otimes 2}}} & \eta_x \Delta x_I & \eta_y \Delta y_I & 0 \\ \eta_x \Delta x_I & \sigma^2_{\beta_{I_{1\otimes 2}}} & 0 & 0 \\ \eta_y \Delta y_I & 0 & \sigma^2_{\gamma_{I_{1\otimes 2}}} & 0 \\ 0 & 0 & 0 & \sigma^2_{\delta_{I_{1\otimes 2}}} \end{bmatrix}_k \quad (6)$$

We have no systematic study of fringe drifting. It is due supposedly to an unidentified moving part in the sndice source or the telescope. We rely on a few image sequences where we observe some sporadic jumps of fringes either in the vertical y or the horizontal x direction. Empirically we can isolate sequences of image stable at the nominal 10^{-4} precision characterizing our measurements. They are separated by a jump observed for all channels simultaneously, either Δx or Δy. The resulting effect due to a feature of CCD readout is seen in Figure 25: first 36 channels are read upwards and last 36 downwards

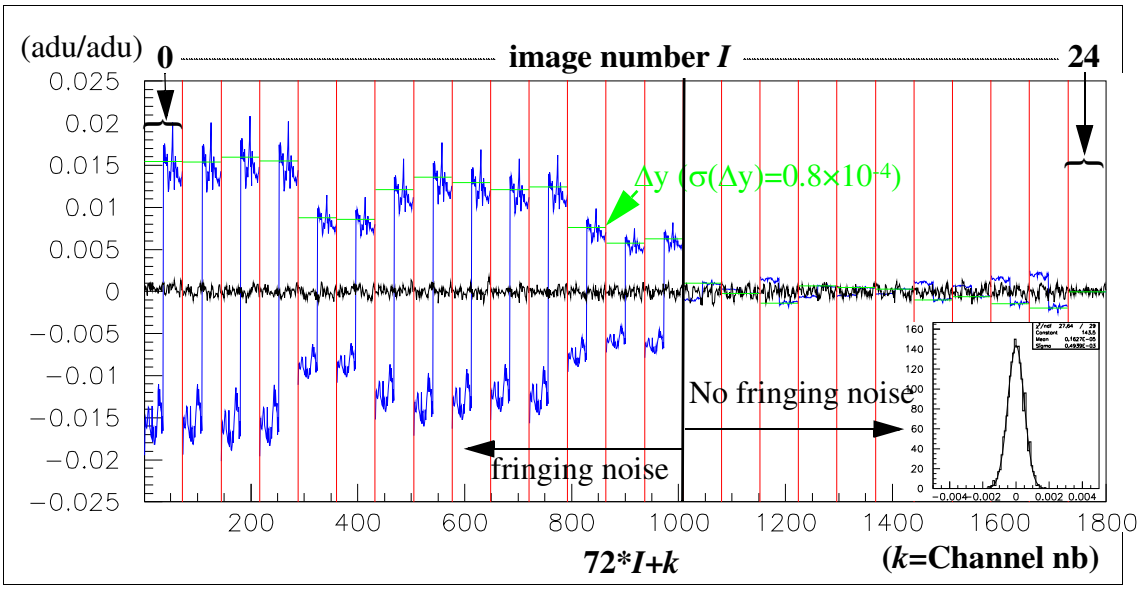

Figure 25: In blue the slope $\eta_y \Delta y$ as a function of channel k and image *I* (η_y fixed to 0 for *I*=24). In black the residual of the fit of this signal with one η_y parameter per channel and one Δy per image. One checks easily that fringing noise seen in Figure 23-b) corresponds to the large Δy shifts. The insert shows the gaussian distribution of the residuals (1 /channel/image) with a 5.10^{-4} rms, yielding a 2% of a pixel size (0.3μ) sensitivity on Δy.

yielding opposite $\eta_y \Delta y$ values for these two groups of channels. Similarly even channels are read rightwards and odd ones leftwards, yielding opposite $\eta_x \Delta x$ values.
The analysis of these results shows that the last 11 images are close enough to be deemed identical for our 10^{-4} criterion, although the fit detects small shifts. The larger shifts seen on the first four images compared to the last eleven ones beeing 15 per mill, the rms error on a Δy measurement done with one channel is 0.5 per mill and done with all 72 channels is 0.06 per mil. Knowing that a one pixel shift yields a 150 adu rms effect, the 96 adu

rms effect on 2 pixels distance seen between first and last images calibrates the Δy scale. We conclude that we have an easy and very precise tool to control the stability of the sndice image and that, with our present apparatus this stability is sufficient to assure that most images can be exactly matched with the ones taken shortly before or after with the same integrated flux Φ_I. The two by two image matrix of 5 can be generalized to a 25 by 25 matrix where each 2 by 2 block is 5. The Figure 29 is just taken from one 1 by 25 row of the big matrix.
The same tools could be applied to the comparaison of same images with different fluxes after scaling all parameters including η_x and η_y with flux ratios. But it needs some technical refinements developed hereafter in §4.3.2

4.3.2 Flux ramp images : PCA or not PCA?

The comparison of two images at the same flux level by the analysis of the joint distribution of pixel values in previous paragraph has much in common with the analysis of pixel to pixel difference presented in §2.5.3. We had to introduce the a small fluctuation of gain Δg and a small displacement Δx,Δy of fringe pattern between two images. The relation between both analyses is the effect of a linear change of variables on the covariance matrix. Comparing two identical images[4] by computing the sum and the difference of pixels amounts to rotating the covariance matrix into its eigensystem with a $\pi/4$ rotation. This is exactly what the principal component analysis method does. More generally comparing two images differing just by a scale factor amounts to a rotation of the covariance matrix.
In the Appendix C, we write the general form of the covariance matrix in equation (C.1). This matrix is obtained by a rotation of angle ϑ which transform the plane (χ,ξ) of the principal components into the (x,y) plane. The (χ,ξ) covariance matrix is diagonal with two eigenvalues σ_1^2 and σ_2^2 (with $\sigma_1^2 > \sigma_2^2$). The rotation which transforms the principal components matrix into an arbitrary covariance matrix is written as:

$$\begin{bmatrix} \sigma_x^2 & \rho\sigma_x\sigma_y \\ \rho\sigma_x\sigma_y & \sigma_y^2 \end{bmatrix} = \frac{1}{1+t^2} \begin{bmatrix} \sigma_1^2 + t^2\sigma_2^2 & t(\sigma_1^2 - \sigma_2^2) \\ t(\sigma_1^2 - \sigma_2^2) & \sigma_2^2 + t^2\sigma_1^2 \end{bmatrix} \qquad t = \tan\vartheta \tag{7}$$

The Figure 26 represents geometrically the ellipses defining the covariance matrix for a sequence of five increasing ϑ angles, together with the analytical form of the corresponding covariance matrix elements using equation (C.4). Knowing the ratio of amplitudes for two images one can rotate the covariance matrix to bring it on the ϑ=0 horizontal form and then fine tune the covariance matrix by a regression analysis. The real optimization of the analysis rely on a modeling of the experimental fluctuations that we called fringing noise. It is done in Appendix C.

[4] differing only because of photon noise

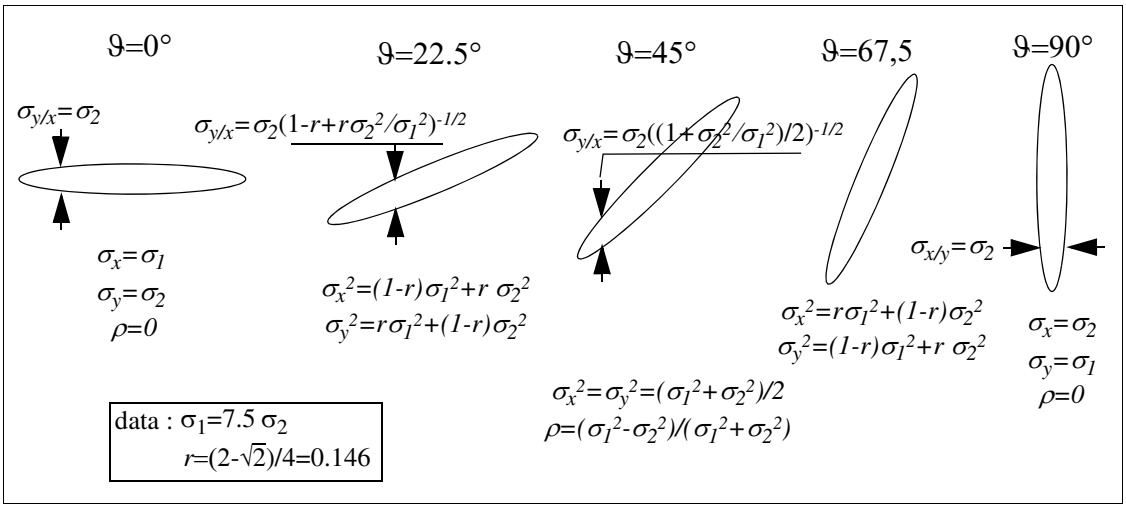

Figure 26: Five ellipses corresponding to five covariance matrices for $\vartheta \in \{0°,90°\}$

4.4 Monitoring algorithms based on a gaussian multivariate image comparison

These algorithms are based on the stability of the sndice-megacam images obtained when both the led light source and the telescope are fixed. It mitigates the effect of the fluctuations of the electronics and the small displacements of the fringes seen in §4.3.1. It uses the two following ingredients :
a) the constitution of classes of pixels called slices with about the same ADC content
b) the results of Appendix C which computes the conditional probabilities of observing a pixel value in a test image when the same pixel fall in a given slice of a reference image.
Prerequisites are needed :
- the definition of an integrated photon flux for each image done in §4.4.1

- the knowledge of the signal/noise ratios found in table 1 telling what type of information can result of the analysis of the covariance matrix [5] depending of the ratio of fluxes of the two images compared using Appendix C.

4.4.1 High precision Integrated flux scale

We have seen in Figure 14 that for a sequence of images at constant led current (few 10^{-5} precision) and with duration fixed electronically (at a microsecond precision) the integrated flux estimator obtained by summing the contents of all CCDs depends only on the LED temperature at a 2×10^{-4} level. A totally independent Hessian flux estimator, compared in Figure 23, agrees with it at a better than 10^{-4} level. We know also from Figure 16 that the same estimators applied to each CCD individually fluctuate by a few per mil because of the gain fluctuations. These observations are reconciled by understanding that the average of 72 channels yield a global flux estimator weighted by the average gain $\Phi_I \times <g_{k,I}>_k$. The average gain fluctuation is divided by the square root of the channel number, i.e. 72. It is notable that this estimator is not sensitive to the fringing noise, that is to the small position mismatches between the telescope and sndice. Therefore it has the potential to extrapolate high precision flux estimation from one

sndice calibration run to the next. What prevents this extrapolation actually is the instability of the electronics.

On the basis of this understanding, we can create an integrated gain×flux scale relating all images of a flux ramp notwithstanding the nature of the varying parameter (duration, LED current or temperature). We demonstrate this method on a calibration ramp consisting of a sequence of 70 images with alternatively varying and current and shutter duration represented in Figure 27. A reference image is chosen at a high illumination

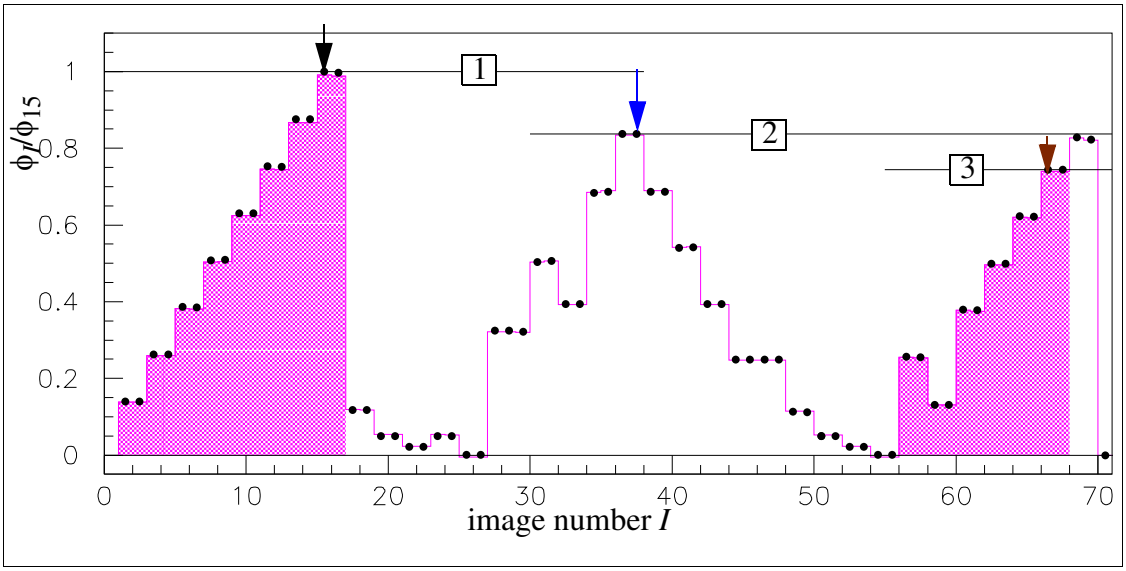

Figure 27: Creation of a common high precision relative flux scale for a 70 images run: 1) three sequences visualized by horizontal lines around a reference image marked by an arrow (black, blue and brown). Relative fluxes within a sequence determined as in Figure 29. 2) The reference image of sequence 2 is measured relative to reference 1 and reference 3 relative to reference 2 and by transitivity all fluxes are related. 3) The two overlap regions 1 over 2 and 2 over 3 yield a set of double determinations. They agree with a discrepancy of 3.10^{-5} rms. The resulting determination of the relative fluxes of all 70 images allow to test the linear model relating integrated flux to exposure time and to LED current. The 28 images marked by shaded area are taken at a common led current with varying exposure and the others at constant exposure with varying led current.

level within each sequence and it is compared to another reference image. Transitively all fluxes are related, doubly measured fluxes providing a precision estimation (3.10^{-5} rms).

4.4.2 precision of ramp control parameters

The high precision of relative flux measurements allows us to test indepently the quality of the two ramping parameters.
First the shutter speed is measured by a light ray interupted by the moving slit. When we fit the shutter time to the fluxes[5] measured in Figure 27, we find the residuals plotted in Figure 28-a. which are compatible with the same led temperature effect as in Figure 14.

[5] taking the images 1-16 and 56-68, all taken with the same led current corrsponding to DAC=410

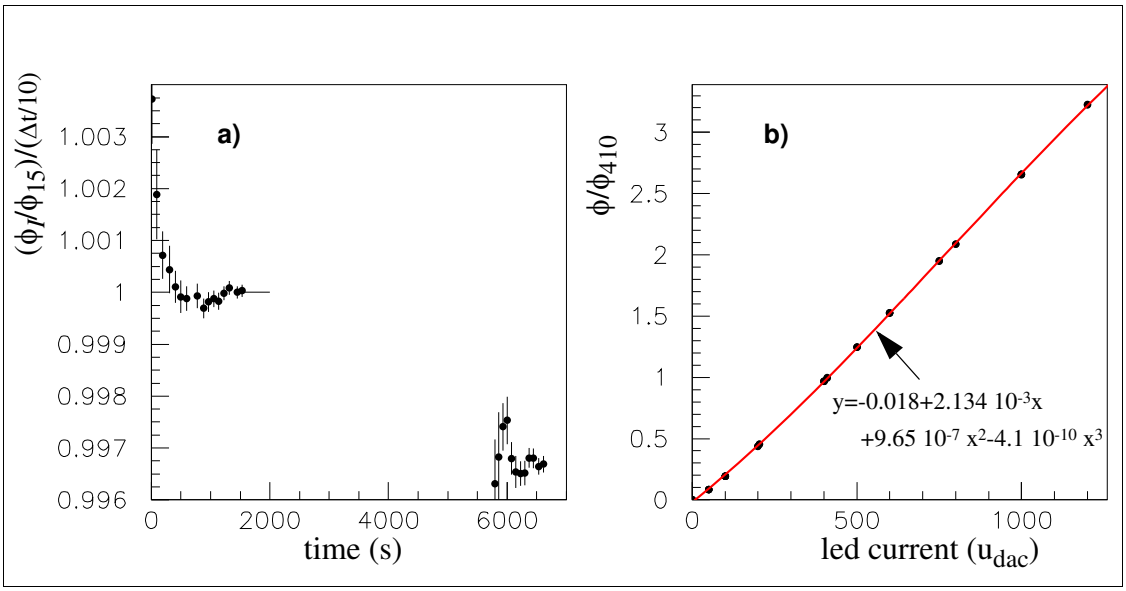

Figure 28: **a)** The variation of the flux/duration ratio for shutter ramp [a] as a function of the exposure time is an effect of led temperature as in Figure 14) ; **b)** Relative flux vs led current for current ramp

a. shutter ramp made of images 1-16 and 56-68 in Figure 27; current ramp of images 17-55

Error bars represent the effect of a one milisecond uncertainty on shutter timing.
Second taking all other images, we can draw in Figure 28-b a led illumination characteristic -flux versus current- compatible with led calibration (a third degree polynomial).
One of our conclusions is that we should preferentially use electronic pulsing, owing to its intrinsic one microsecond resolution. Another conclusion is that in order to reach a precision on flux measurement as good as allowed by the high photon statistics a lot of precautions are needed depending on the detailed pixel summing algorithm. In case of a simple pixel sum dubious pixels such as dead columns have to be corrected for. The pixel to pixel comparison detailed in next paragraph is more robust because bad pixels are filtered automatically and photons migration between neighbour pixels is accounted for. using fringe position estimators Δy and Δy (in Figure 25).

4.5 The pixel to pixel image comparison

The method introduced above in §4.3 was applied to a sequence of images at constant level to study the reproducibility of the system Sndice-CFH-Megacam and the perspectives of a high precision monitoring system. This method can be applied as such to an illumination level ramp such as the one studied in the previous paragraph.
For each electronic channel we divide the pixel content distribution in one hundred slices (each 32 adu wide), totalizing a $\pm 1.5\ \sigma$ interval around the mean. This mean illumination of the channel is obtained by a gaussian fit to the adc content distribution.
Then for each slice, each channel, each filter and each image, the adc content is histogramed and the mean and the RMS of all histograms are kept in different vectors.

4.5.1 The sum filter

The $\Sigma_x \times \Sigma_y$ filter degrades the original x×y image resolution by a factor 2 and improves the photon count by a factor 4. It is easy to understand how this process relates the reference image to a current image in a sequence:
Figure 29 relates the adc counts in given pixels of a reference image (a 6 s exposure) and

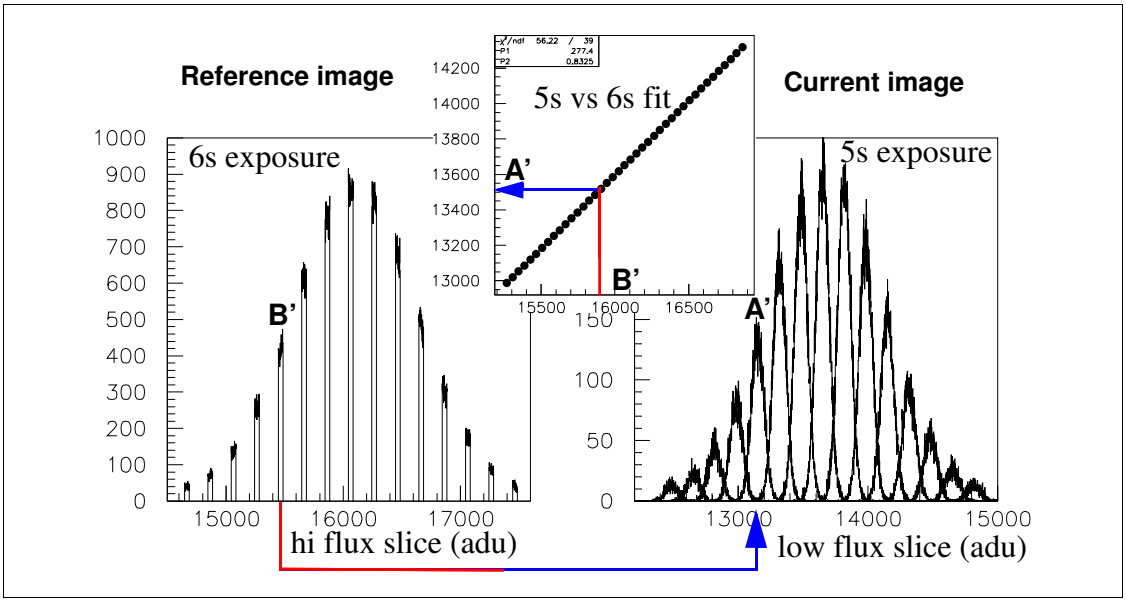

Figure 29: Rectangular slices in the pixel count of 6s reference image (left) are transformed by Poisson noise into gaussian in the 5s current image(right). Only one every five slices is represented. The mean values and width of the current image slices are fitted as a linear function of mean value of the reference image slices as shown in the insert on top. The distribution of residuals is shown in Figure 30. These images are part of a sequence ramping the exposure time at a fixed led current.

the counts in the same pixels in another image (at a 5 s exposure in this example or at any other exposure). At first order the two parameters of the linear fit -the central point and the slope- are two independent determinations of the ratio of exposition times, e.g. the ratio 5÷6 in Figure 29. At second order the central point measures the integral linearity and the slope the differential linearity. In principle, as shown in Appendix B, comparing both ratios would check the linearity of the opto-electronic chain. However, as seen in Figure 36, the differential linearity estimator is biased and it has to be corrected.

The Figure 30 shows the residuals of the linear fit shown in Figure 29 which relates the photon counts in a given quadruplet of a reference image and of a current image. The fit includes 40 points with individual error bars $\sigma/\sqrt{N}$ in a 0.2-0.4 adu range[6], computed considering photon statistics as the unique noise source. The dispersion of residuals in Figure 30 b) is 0.4 adu compared to these 0.2-0.4 adu. This leaves little place for an extra noise either electronic or optical. We know that for the tails of the ADC distribution outside a ±2 σ cut the residuals are much bigger. This is understood because these tails

[6] σ=31 adu (cf.Figure 31) and the number of quadruplet/slice N=24000 at center and N=6000 at ±1.5 σ

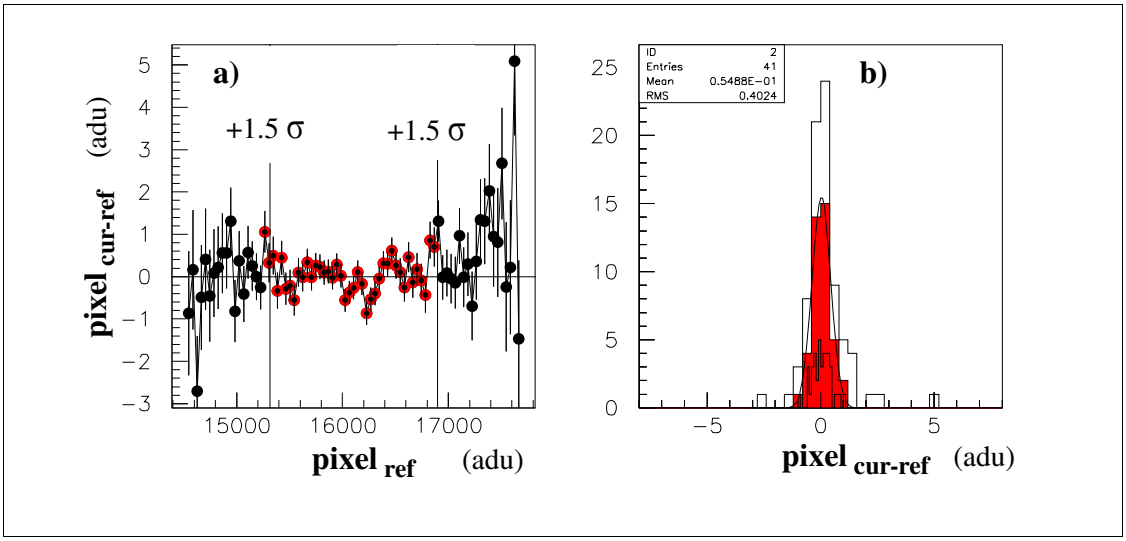

Figure 30: Residuals of the linear fit of Figure 29 : a) as a function of pixel count in reference image; b) projected on an histogram, it yields a 0.4 adu RMS dispersion. In red the points included in the fit on the condition that they are in a ±1.5 σ interval around most probable pixel value. Error bars are computed for a pure Poisson photon noise.

are due to a few large optical defects which are unstable from one image to the next. We keep systematically the estimate of the dispersion of residuals with the fit estimates in our data base, as an estimator of extra noise.

With the point to point errors well controlled, we can examine the precision of the parameters obtained by the fit. If the point to point fluctuations are uncorrelated as Poisson's are, the constant term error is roughly divided by the square root of number of points ($\sqrt{40}$) and if they are correlated we have to be more prudent but the RMS of residuals is a worse case limit. The constant term being around 13,000 adu (for 15,000 adu) and the residuals being 0.4 adu (rms), the relative error is $<<0.3\text{x}10^{-4}$. For the slope the conservative fitting error based on RMS of residuals is below $8\text{x}10^{-4}$ adu/adu to be compared with the $8\text{x}10^{-4}$ measured on Figure 36.

For the classical description of the electronic transfer function by a single gain parameter for each electronic channel, both linear fit parameters yield independent gain estimates. When we compare both gain estimates, the check fails by more than one order of magnitude compared to the error estimates.

4.5.2 The double derivative and the gradient filters

In paragraph §4 we introduced a third measurement of the electronic gain based on the photon statistics which drive the fluctuations of the double derivative filter. Here again the $\Delta_x \times \Delta_y$ fit seen in Figure 31 yields a third gain estimator, which will help solving the discrepancies affecting the two gain estimators. It was shown in that earlier analysis that this noise estimator was more sensible but less sensitive that the usual gain estimators based on the $\Sigma_x \times \Sigma_y$ fit (i.e. those discussed in Figure 29 and Figure 30).

We shall be guided by the paragraph §4 on the way to use all four filters to complete the description of the images and their fluctuations. fits per electronic channel and per image provided by our algorithm. We shall also compare the new method with the old one

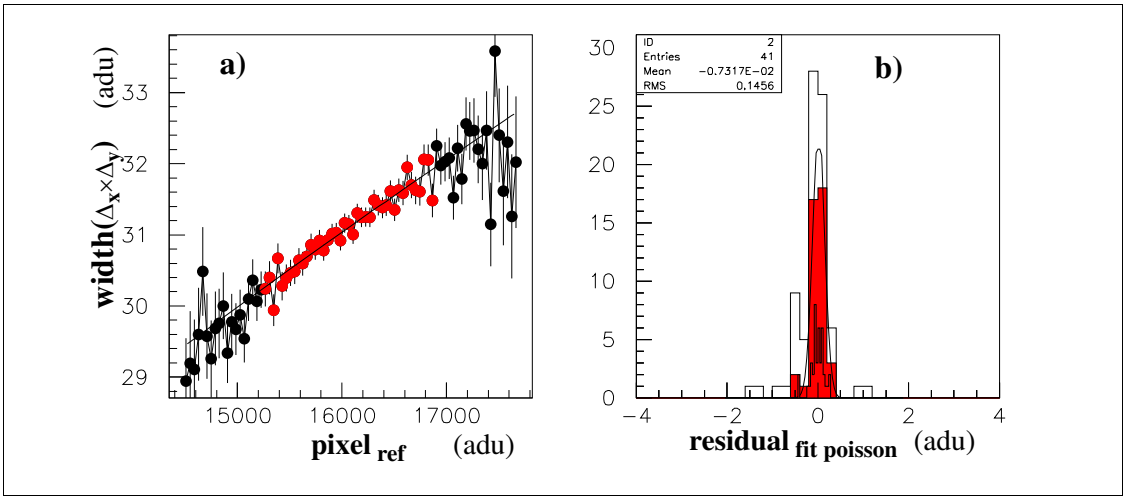

Figure 31: **a)** Fit of the Hessian filter RMS $\sigma(\Delta_x \times \Delta_y) \sim \sqrt{N_\gamma}$ as a function of the mean pixel content $\langle \Sigma_x \times \Sigma_y \rangle \sim N_\gamma$ inside a 1.5 σ cut.
b) Residuals of the previous fit. To our best knowledge, the point to point fluctuations are driven only by the photon statistics.

consisting in histogramming not only current image pixels such as in Figure 29 but also the difference between corresponding pixels of current image and reference image affected by a constant weight (which was almost what was done in the old method). This doubles the number of fits, but the new data are mostly redundant.

•References

1 E.Barrelet and K.Schahmaneche; Testing Megacam with SNDICE; LPNHE 2010-04

2 A.Guyonnet, Thesis Université Denis Diderot; 27/09/2012

3 C.Juramy, Thesis

4 E.Barrelet; Digital Image Processing for SNDICE; LPNHE 2010-06

5 G.Sapiro, Geometric Partial Differential Equations and Image Analysis, Cambridge University Press, 2006; ISBN-10: 0521685079; ISBN-13: 978-0521685078

Appendix A- CCD readout electronics

1. **General**
   electrometer, charge transfer, floating gate, charge sensing amplifier,
2. **Megacam readout**
   The characteristic features of the Megacam electronics are seen in Figure 32. It

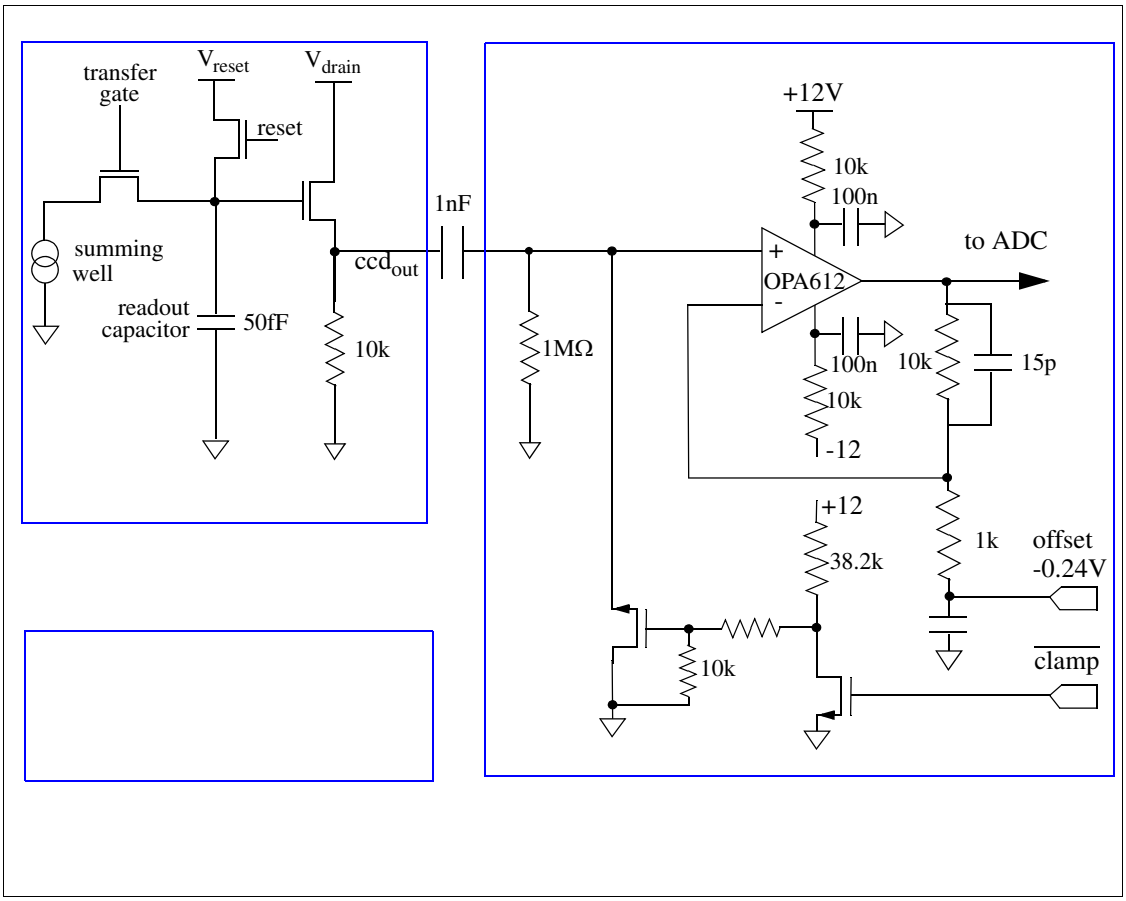

Figure 32: Schematics of Megacam CCD readout

consists in freezing the DC level of the amplifier input (using the 'clamp' command) while the preamplifier input level (inside the CCD) is frozen in the reset state following the readout of pixel n-1. It is worth remembering that this CCD reset level is varying randomly due to so-called KT/C noise with an amplitude corresponding to a few hundreds e^- and that the CCD preamplifier output is not refered to ground. In a nutshell: clamping has two functions -DC restore and KTC noise suppression-. In a report (LPNHE 2004-11), we have shown that this method has only advantages compared to others[7]. In particular we have demonstrated and checked experimentally that the clamping noise is 0.5 e^- only. This digitization

[7] Historically correlated double sampling scheme was introduced for suppressing low frequency system noise (60hz). For megacam pickup immunity comes from the proximity of detector and electronics within a common shield

method could be made exceptionally robust with amplitude measurement depending only on the timing of one clock (convert) and not at first order. However the features observed on SNDICE flat field images (§3.2) and the behaviour of overscan data (§2.4.1 and §2.4.2) might be related with megacam peculiar clocking scheme[8].

3. **Optimum readout**
   Their basis rests on the assessment of recent technological developments which give an easier access to high precision photometry:

1. Low noise MOS circuitry: as demonstrated in [3], we can make a FET which have both a negligible gate leakage current and an optimal input noise figure. This permits to perform a baseline restoration not for all pixels like megacam does but only for each line. The double gain feature also demonstrated in [3] permits an integration of the full digitization chain on a single circuit powered at 5 volts.
2. Digital filtering: as also demonstrated in [3], it permits a true correlated double sampling measurement of each pixel with an optimal filtering and an optimal readout time.
3. Large scale integration which can make a good use of the digital data.

Adding to those, the technological progresses which have lead to the construction of the Sndice light source, namely:

1. High quantum efficiency LEDs.
2. Gamut of LEDs covering the bandwidth of the CCD detector.

Commercial chips -DAC and ADC- with a real 16 bits accuracy.

Appendix B- Cumulating non-linearity and instability of image digitization

The model of the transfer function given in equation 2 is fully linear. We could test a weaker sort of linearity in which integral linearity and differential linearity are slightly different using two exposures at different fluxes and comparing as sketched in Figure 33 the integral response (pedestal to mean flux) and the differential response (10% interval around the mean). The statistical precision is around 10^{-5} for the integral measurement and 10^{-4} for the differential one, but the fluctuations of gain are much larger ($5x10^{-3}$ in Figure 16). If we suppose that the fluctuations of gain leave the ratio of differential to integral gain constant as in Figure 33 (homothetic transfer function), we can test the linearity of the transfer function to the level of precision of the differential gain.
The situation is complicated by another effect due to the bias of the differential gain measurement due to the statistical fluctuation of the signal. This is discussed in Appendix C. Figure 36 shows that differential gain and integral one are the same within

[8] The few per mil precision obtained is well within megacam specifications but it falls short of the 10^{-4} precision convenient for the present sndice analysis. We consider as megacam clocking scheme what is described in a DSM-DAPNIA memo (H.Deschamps 28/03/02 - Private communication).

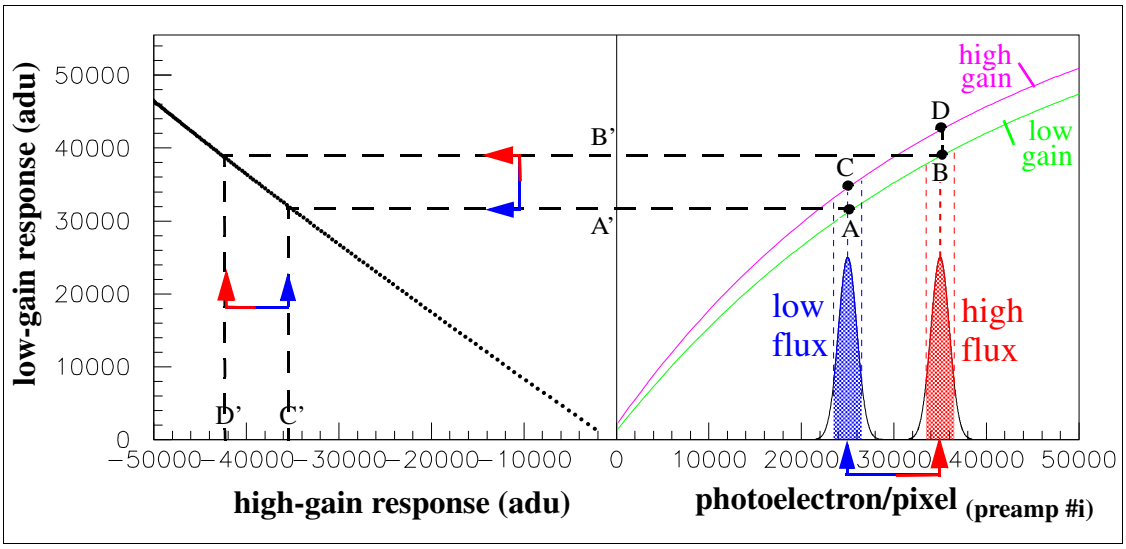

Figure 33: Representation of the responses of the channel #i when both gain and flux may change between two images. The change of flux is visualized by a red-blue arrow and an A↔B exchange on the low gain photoelectric response (or C↔D on the high gain). The corresponding

a dispersion of $5x10^{-4}$.

We conclude that we can assume full linearity for all electronic channels at this $5x10^{-4}$ precision level. This is not terribly surprising since our measurements are restricted to about 10% of CCD full well range. The measurement of non linearities using the same method could be more precise by an order of magnitude if the gain of the electronis were stable.

Appendix C- Using bivariate gaussian variables to compare two images

In paragraphs 4.2 and 4.3 we introduced multivariate gaussian distributions (288 dimensions per image). It can be projected on a two dimensional space by selecting one channel, one filter and two images. The couple of ADC values taken by a given CCD channel in these two images with an identical Sndice illumination is represented as the outcome of a 2-d random vector variable $\{X,Y\}$ which mean is $\{<X>,<Y>\}$ and which covariance matrix is $\boldsymbol{C}$. $\boldsymbol{C}$ is defined by the 3 measurable parameters σ_x , σ_y and ρ. Let us recall here three basic representations of a 2-d gaussian variable.

The first representation is defined by the mean and the covariance matrix $\boldsymbol{C}$ parametrized by σ_x , σ_y and ρ (cf. 2). The probability is given by 3.

The second representation is the principal component representation parametrized by σ_1^2 and σ_2^2 and ϑ. The principal components σ_1^2 and σ_2^2 are the two eigenvalues of $\boldsymbol{C}$ and ϑ is the rotation angle transforming the eigen matrix into $\boldsymbol{C}$. Formulas passing from the first to the second representation are C5 and C6 and reciprocally C7.

The third representation is the regression representation where the bivariate law $Pb(X \cup Y)$ is decomposed into the product $Pb(Y|X)*Pb(X)$, both terms being gaussian

laws of one variable defined by the three parameters σ_x, $\alpha_{y/x.}$ and $\sigma_{y/x.}$. The formulas relating the first representation and the third are found in 9.

1. Covariance matrix algebra

The covariance matrix of the gaussian random variables x and y is a 2⊗2 symmetric matrix:

$$\boldsymbol{C} = \begin{bmatrix} \sigma_x^{\,2} & \rho\sigma_x\sigma_y \\ \rho\sigma_x\sigma_y & \sigma_y^{\,2} \end{bmatrix} = \sigma_x^{\,2} \times \begin{bmatrix} 1 & \rho\alpha \\ \rho\alpha & \alpha^2 \end{bmatrix} \qquad \begin{matrix} \rho \le 1 \\ \sigma_y \le \sigma_x \rightarrow \alpha \le 1 \end{matrix} \tag{C.1}$$

The inverse of this covariance matrix is:

$$\boldsymbol{C}^{-1} = \frac{\sigma_x^{\,-2}}{1-\rho^2} \times \begin{bmatrix} 1 & -\rho\alpha^{-1} \\ -\rho\alpha^{-1} & \alpha^{-2} \end{bmatrix} \tag{C.2}$$

The probability of density of the 2d gaussian variable (a «bivariate normal law») is:

$$f(x,y) = \frac{1}{2\pi\sigma_x\sigma_y\sqrt{1-\rho^2}} e^{-\frac{1}{2}(\tilde{V})\boldsymbol{C}^{-1}\vec{V}} \qquad \vec{V} = \begin{bmatrix} x - \langle x \rangle \\ y - \langle y \rangle \end{bmatrix} \tag{C.3}$$

The eigenvalue equation of the C matrix is :

$$\lambda^2 - (1+\alpha^2)\cdot\lambda + (1-\rho^2)\cdot\alpha^2 = 0 \tag{C.4}$$

The two solutions of this eigen value equation are :

$$\lambda^{\pm} = \frac{1}{2}\left\{(1+\alpha^2) \pm \sqrt{(1-\alpha^2)^2 + 4\alpha^2\rho^2}\right\} \qquad \begin{matrix} \sigma_1^2 = \lambda^{+} \\ \sigma_2^2 = \lambda^{-} \end{matrix} \qquad \sigma_2 < \sigma_1 \tag{C.5}$$

Two corresponding eigenvectors $V^{\pm}$ are :

$$V^{\pm} = \begin{bmatrix} 1 \\ \tan\vartheta^{\pm} \end{bmatrix} = \begin{bmatrix} 1 \\ \sqrt{1+r^2} \mp r \end{bmatrix} \qquad \begin{matrix} r = (1-\alpha^2)/2\rho\alpha \\ \vartheta^{+} = \operatorname{atan}(\sqrt{1+r^2} - r) \end{matrix} \tag{C.6}$$

The covariance matrix in the eigen system is diagonal. This system is also called the principal components system. The inverse rotation of angle ϑ which transforms the eigen matrix into an arbitrary covariance matrix can be written as:

$$R(\vartheta)\otimes\begin{bmatrix}\sigma_1^2 & 0\\ 0 & \sigma_2^2\end{bmatrix}\rightarrow\begin{bmatrix}\sigma_x^2 & \rho\sigma_x\sigma_y\\ \rho\sigma_x\sigma_y & \sigma_y^2\end{bmatrix}=\begin{bmatrix}\frac{\sigma_1^2+\sigma_2^2}{2}+\cos 2\vartheta\frac{\sigma_1^2-\sigma_2^2}{2} & \sin 2\vartheta\frac{\sigma_1^2-\sigma_2^2}{2}\\ \sin 2\vartheta\frac{\sigma_1^2-\sigma_2^2}{2} & \frac{\sigma_1^2+\sigma_2^2}{2}-\cos 2\vartheta\frac{\sigma_1^2-\sigma_2^2}{2}\end{bmatrix}$$

which can be made more compact by expressing cos 2ϑ & sin 2ϑ as function of t=tan ϑ :

$$\begin{bmatrix}\sigma_x^2 & \rho\sigma_x\sigma_y\\ \rho\sigma_x\sigma_y & \sigma_y^2\end{bmatrix}=\frac{1}{1+t^2}\begin{bmatrix}\sigma_1^2+t^2\sigma_2^2 & t(\sigma_1^2-\sigma_2^2)\\ t(\sigma_1^2-\sigma_2^2) & \sigma_2^2+t^2\sigma_1^2\end{bmatrix} \qquad (C.7)$$

The equality of the two matrices in 7 connects the first and the second representation of the bivariate gaussian law mentioned above. In 9 we shall connect them with the third representation. Symbolically the relations between the 3 parameters defining each representation is figured in 8.

$$\begin{bmatrix}\sigma_1\\ \sigma_2\\ t\end{bmatrix}\leftrightarrow\begin{bmatrix}\sigma_x\\ \sigma_y\\ \rho\end{bmatrix}\leftrightarrow\begin{bmatrix}\sigma_x\\ \sigma_{y/x}\\ \alpha_{y/x}\end{bmatrix} \qquad (C.8)$$

PCA *Covariance* *Regression*

2. Linear regression algebra:

Linear regression analysis is commonly used as an empirical method. However it is based on the exact mathematical properties of the bivariate gaussian law illustrated in Figure 34. Two dimensional gaussianity implicates that the conditional law in X is a

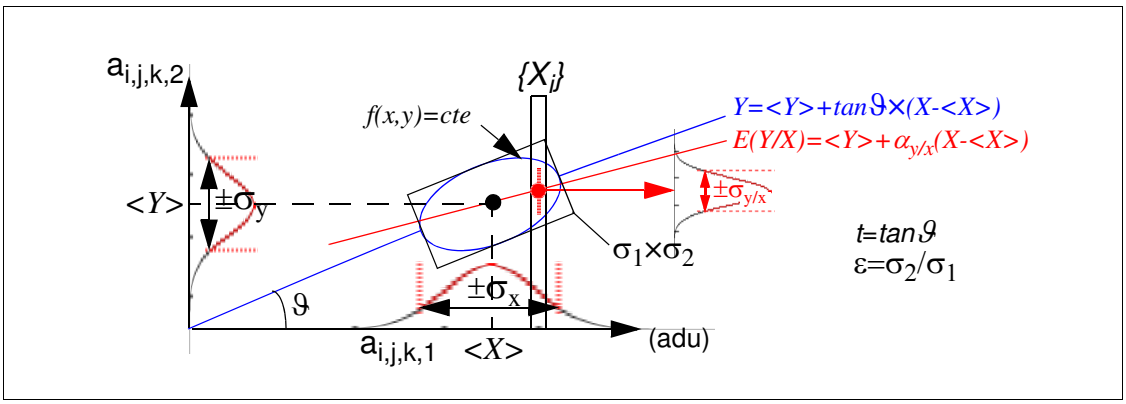

Figure 34: Histogramming the content of pixel $a_{i,j,k}$ in image 1 versus the same in image 2. The constant probability ellipse (blue) has semi-axes σ_1 and σ_2, an inclination $t=tan\vartheta$ and an aspect ratio ε. The conditional probability is a 1-d gaussian (red) of mean E(Y/X)=<Y>+ $\alpha_{y/x}$(X-<X>) and of constant width $\sigma_{y/x}$.

gaussian which width $\sigma_{y/x}$ is independent of X and which mean is a linear function of X of slope $\alpha_{y/x}$ as seen in equation 9. Reciprocally this property of the conditional law

implies that the bivariate law is gaussian. The comparison of two sndice images based on the extremely high number of pixel (4.6×10^6) and the number of photon inside a pixel ($2.\times10^4$) yield for each digitization channel a high statistical accuracy relevant of a mathematically defined precision, rather than an empirically estimated approximation.

$$\begin{cases} E(Y/X) = \langle Y\rangle + \alpha_{y/x}(X - \langle X\rangle) \\ \sigma(Y/X) = \sigma_{y/x} \end{cases} \qquad \begin{cases} \alpha_{y/x} = \rho\sigma_y/\sigma_x = t(1-\eta^2)/(1+(t\eta)^2) \\ \sigma_{y/x} = \sigma_y\sqrt{1-\rho^2} = \sigma_1\eta\sqrt{\dfrac{1+t^2}{1+(t\eta)^2}} \\ \sigma_x = \sigma_x = \sigma_1\sqrt{\dfrac{1+(t\eta)^2}{1+t^2}} \qquad \eta = \dfrac{\sigma_2}{\sigma_1} \end{cases} \quad \text{(C.9)}$$

One checks easily that the regression line is the locus of vertical tangents to the ellipses defined by *f(x,y)=cst* in 3. Identically one gets the slope $\alpha_{x/y}$ of *E(X/Y)* as a linear function of *Y* by exchanging the role of x and y. The equation 9 allows to pass from the covariance representation to the regression representation. The invariants of covariance matrix C give some help or some checks in establishing algebraic formulas.

$$\begin{aligned} Tr(C) &= \sigma_x^2 + \sigma_y^2 = \sigma_1^2 + \sigma_2^2 \\ \sqrt{|C|} &= \sigma_x\sigma_y\sqrt{1-\rho^2} = \sigma_{y/x}\sigma_x = \sigma_{x/y}\sigma_y = \sigma_1\sigma_2 \end{aligned} \quad \text{(C.10)}$$

3. Parametric estimation of multivariate gaussian variables:

Among the three different systems of 3 parameters, for each bivariate gaussian (or quasi-gaussian) we have to make a choice. The choice can depend on the couple of variables (filters) considered, their range, their noise, but also on the data processing algorithm and on the non-gaussian features which can play a role at second order.

a) Comparison of algorithms : the covariance algorithm is defined by a sum of 10^{13} terms! [9]. This is not workable. But, as X and Y are digitized on a range smaller than 10^3 adu's, the practical computation goes by histogramming the 4.6×10^6 (X,Y) pairs for each of the 72 channels. The effective histogram size is below 10^6 bins for any filter. The covariance sum is rearranged as a weighted sum of histogram bins . This technique works for the 3 parameters systems envisaged. However it works best with regression where it consists in recording 1-d conditional histograms.

b) Non-gaussian tails : they show up in the projection along the principal component σ_1 axis (cf. Figure 11a&Figure 12), not along the perpendicular σ_2 axis (cf. Figure 15a) which senses the variation of content of a pixel from one exposure to the other.

For the filter α non-gaussian tails are eliminated by a ±1.5 rms cut around the mean value. For β,γ and δ filters the cut is at ±2.2 rms.

c) Variable conditional law : For a pure bivariate gaussian law the conditional law giving the distribution of *Y* (a pixel of image 2) in a narrow slice of *X* (a pixel of image 1) is

[9] $\sum_{ij}(X_i-\langle X\rangle)\times(Y_j-\langle Y\rangle)$

fixed by 9. It is well understood that there is a slight deviation from 9 due to the fact the average number of photon per pixel is increasing linearly with *X*. This effect is precisely measured owing to a good *X* resolution (narrow slices and high statistics), as a function *f(X-<X>)* (replacing 9 by 11):

$$\sigma^2(Y/X) = \sigma^2_{y/x} + f(X - \langle X\rangle) = \sigma^2_y(1-\rho^2) + f(X - \langle X\rangle) \qquad f(0) = 0 \qquad \text{(C.11)}$$

In case of a pure Poisson noise the function *f(X)* is linear (*f(X)=X×G×<Y>/<X>*). It is normalized by the gain*efficiency coefficient $G=N_\gamma/<Y>$ expressed in photon per adu unit. In reality the variance *f(X)* is not perfectly proportional to *X*. But it can be represented by a second degree polynomial[10].

d) Optimal parametric estimation method : We came to the conclusion that the best estimation method consists in fitting perfect gaussian conditional laws independently for any slice of the *X* variable while letting width and mean vary with *X*. In fact we shall fit systematically either first degree or second degree polynomials in *X* on both σ^2*(Y/X)* and *E(Y/X)* for the *X* interval which excludes non gaussian tails. The central values, i.e. the constant term in the polynomial fit as a function of *X-<X>*, are the one chosen to apply 9. If ellipticity is large (ε <1%) $\alpha_{y/x}$ estimates the inclination t and $\sigma_{y/x}$ estimates noise fluctuation ε. At our high precision 10^{-4}, we need to take into account the cross terms seen in 9.

4. Building a covariance matrix from various error laws affecting pixel counts:

a) Fringing : The distribution of the pixel content in image 1 due to the interference between specular and diffuse reflection is approximately gaussian with a width σ_F. The joint 2-d distribution of two proportional images 1 and 2 with a gain×flux×efficiency ratio α_{21} and no noise is modelled by a bivariate normal distribution with projected widths $\sigma_x=\sigma_F$, $\sigma_y=\sigma_F\times\alpha_{21}$, and a correlation coefficient $\rho_F=1$.

However we can model the effect of the «fringing noise» (due to the motion of the interference pattern from image 1 to image 2) by introducing in the antidiagonal terms of the covariance matrix a correlation coefficient $\rho_F \le 1$. The fringing covariance matrix, without Poisson or electronic noise, is C_F.

$$\boldsymbol{C}_F = \sigma_F^2 \begin{bmatrix} 1 & \rho_F\alpha_{21} \\ \rho_F\alpha_{21} & \alpha_{21}^2 \end{bmatrix} \qquad \begin{array}{l} Image\ ratio \overline{\frac{2}{1}} \leftrightarrow \frac{\sigma_y}{\sigma_x} = \alpha_{21} = \alpha_{12}^{-1} \\ Fringing\ \ noise \leftrightarrow \rho_F < 1 \end{array} \qquad \text{(C.12)}$$

The conditional law of fringing is defined by 13:

$$\begin{array}{ll} \alpha_{Fy/x} = \alpha_{21}\rho_F & \sigma^2_{Fy/x} = \alpha^2_{21}\sigma^2_F(1-\rho^2_F) \\ \alpha_{Fx/y} = \alpha_{12}\rho_F & \sigma^2_{Fx/y} = \sigma^2_F(1-\rho^2_F) \end{array} \qquad .\rho_F = \left(1 - \frac{\sigma^2_{Fy/x}}{\alpha^2_{21}\sigma^2_F}\right)^{1/2} \qquad \text{(C.13)}$$

[10] the constant term is the «pedestal noise», the second degree term is a «gain noise»

The eigensystem of a simple system with fringing, but no noise either from fringing or from electronics, is defined by 4 and 5. They yield $\vartheta^{+}=\arctan(\alpha_{21})$ and $\vartheta^{-}=\vartheta^{+}+\pi/2$. This transform consists, knowing the gain ratio $\alpha=\alpha_{21}$, in subtracting or adding the gain corrected image 2 from image 1. It is expressed by the orthogonal matrix Ω, which transforms C_F of 12 , into C_F' 14 :

$$\boldsymbol{C}_F \xrightarrow{\Omega} C_F' = \sigma_F^2\left(\begin{bmatrix}1+\alpha^2 & 0\\ 0 & 0\end{bmatrix} + \frac{1-\rho}{1+\alpha^2}\begin{bmatrix}-2\alpha^2 & \alpha^2-1\\ \alpha^2-1 & 2\alpha^2\end{bmatrix}\right) \qquad \Omega = \frac{1}{\sqrt{1+\alpha^2}}\begin{bmatrix}1 & -\alpha\\ \alpha & 1\end{bmatrix} \tag{C.14}$$

$$\left\|C_F'\right\|_{22} = \frac{2\alpha^2\sigma_F^2(1-\rho)}{1+\alpha^2} = \frac{2}{(1+\rho)}\cdot\frac{\sigma_{Fy/x}^2}{1+\alpha^2}$$

We see that this covariance matrix is diagonal only if $\rho=1$ (no fringing noise) or if $\alpha=1$ (same level images). Figure 35 illustrates the fact that, when these two conditions are not

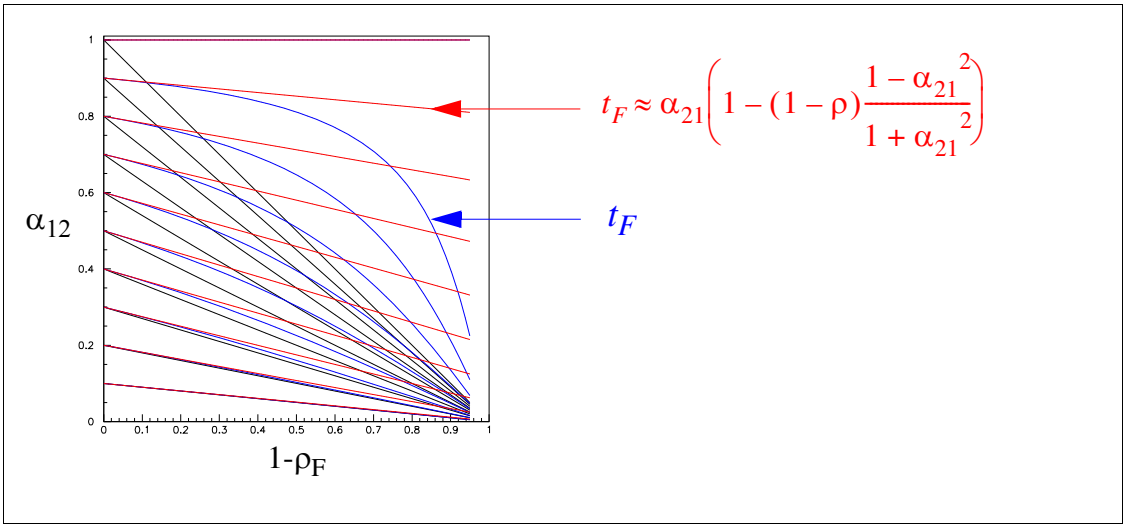

Figure 35: Correlation of images 1 and 2 : slope t_F (blue) of the principal axis as a function of the fringing noise $x=1-\rho_F$ and gain ratio α_{21} and its first order approximation in x (red).

met, the slope of the PCA system is not equal to the gain×flux ratio α_{21} while the slope of conditional law is still expressed by $\alpha_{21}\rho_F$ from 13. We see equally in 14 that considering the effect of the shift of fringes from image 1 to image 2 as a gaussian noise[11], the rms effects of this noise computed by two methods are related as they should be :

1. as the width $\sigma_{Fy/x}$ of the conditional law
2. as the corresponding diagonal term $\|C_F'\|_{22}$ in eigen matrix

b) Electronic noise : Fluctuations due to Johnson noise in the amplifier and pedestal noise (not dependent of image) or to Poisson noise (proportional to square root of the

[11] This implies that ρ_F is close to 1

flux in image i) or to the system noise (relative to the gain×flux×efficiency signal in image i) are independent in both images. They yield no antidiagonal correlation term:

$$\boldsymbol{C}_{xy} = \begin{bmatrix} \delta_x^2 & 0 \\ 0 & \delta_y^2 \end{bmatrix} \qquad \begin{aligned} &Johnson \leftrightarrow \delta_x^2 = G^2 n_0^2 \qquad \delta_y^2/\delta_x^2 = 1 \\ &Poisson \leftrightarrow \delta_x^2 = G^2 N_\gamma \qquad \delta_y^2/\delta_x^2 = \alpha_{21} \\ &GainFlux \leftrightarrow \delta_x^2 = (\varepsilon G N_\gamma)^2 \qquad \delta_y^2/\delta_x^2 = \alpha_{21}^2 \end{aligned} \tag{C.15}$$

Each source of noise yield a specific covariance matrix C_{xy}. All matrices are added to C_F to yield the general covariance matrix $\boldsymbol{C}$ detailed in 1 :

$$\boldsymbol{C} = \begin{bmatrix} \sigma_x^2 & \rho\sigma_x\sigma_y \\ \rho\sigma_x\sigma_y & \sigma_y^2 \end{bmatrix} = \begin{bmatrix} \sigma_F^2 + \Sigma\delta_x^2 & \rho_F\sigma_F^2\alpha_{21} \\ \rho_F\sigma_F^2\alpha_{21} & \alpha_{21}^2\sigma_F^2 + \Sigma\delta_y^2 \end{bmatrix} \tag{C.16}$$

It is useful to express this covariance matrix in the system where the y coordinate is the difference both equalized images, as we did in the special case of pure fringing noise (see 14).

$$\boldsymbol{C} \rightarrow C' = C_F' + \frac{1}{1+\alpha^2} \begin{bmatrix} \Sigma(\delta_x^2 + \alpha^2\delta_y^2) & \alpha\Sigma(\delta_y^2 - \delta_x^2) \\ \alpha\Sigma(\delta_y^2 - \delta_x^2) & \Sigma(\alpha^2\delta_x^2 + \delta_y^2) \end{bmatrix} \tag{C.17}$$

There are only three measurable quantities in a square symmetric 2×2 matrix like $\boldsymbol{C}$ when we want to determine all the parameters of realistic noise model. The non diagonal terms vanish when we compare similar images. The upper left term $\|C'\|_{11}$ depends on the of the fringe intensity and the lower right one $\|C'\|_{22}$ depends on the noise, as it should be. In order to fix the noise model explicitly we have to check the hypotheses concerning all noise parameters on this single $\|C'\|_{22}$ term. For that we must choose different couple of images and couple of filters with different properties. But we will first check this method against the one using the conditional probability width $\sigma_{y/x}$.

We check the conformity of the 2-d distribution obtained for each electronic channel to the bivariate normal probability law by a two step fitting procedure:
1) firstly fitting a 1-d gaussian distribution of image 2 content *(Y)* for each value of the image 1 content *(X) (cf.* Figure 24*)*. This yields two sequences: conditional means <*Y/X*> and rms (or variances) σ*(Y/X)* as a function of *X*.
2) secondly fitting a linear relation between the mean <*Y/X*> and the variance σ^2*(Y/X)* and *X* (cf.Figure 29).
The quality of these fits is excellent (residuals seen in Figure 30). They give our basic estimators :
The slope $\alpha_{y/x}$ of the <*Y/X*> versus *X* fit is given for a normal variable by 9, where $\alpha_{y/x} = \rho\sigma_y/\sigma_x$. Using 16 and the linearity condition of 12, we get:

$$\alpha_{y/x} = \rho_F \frac{\alpha_{21}\sigma_F^2}{\sigma_x\sigma_y} \cdot \frac{\sigma_y}{\sigma_x} = \alpha_{Fy/x} \frac{\sigma_F^2}{\sigma_F^2 + \Sigma\delta_x^2} \qquad \begin{aligned} \alpha_{y/x} &= \alpha_{Fy/x}(1 + \Sigma\delta_x^2/\sigma_F^2)^{-1} \\ \alpha_{x/y} &= \alpha_{Fx/y}(1 + \Sigma\delta_y^2/\alpha_{21}^2\sigma_F^2)^{-1} \end{aligned} \quad \text{(C.18)}$$

Equation 18 expresses the difference between the slope of the regression line $\alpha_{y/x}$ and the ratio (image 1/image2) of pixel counts α_{21}. This is a bias in the estimation of the gain×flux ratio which is commonly overlooked. Its origin is schematized in Figure 34. The fringing noise is introduced by 1- ρ_F and the other noises, mostly electronic, by the δ_x/σ_F terms. If the fringes in images 1 and 2 were not correlated (ρ_F=0) the correlation coefficient $\alpha_{y/x}$ would be null and therefore not give an information on the gain ratio.
Similarly we compute the rms $\sigma_{y/x}$ of the conditional probability using the covariance matrix of 16 and the definitions of 13 :

$$\begin{aligned} \sigma_{y/x}^2 \cdot (\sigma_F^2 + \Sigma\delta_x^2) &= \sigma_F^2 \cdot (\sigma_{Fy/x}^2 + \Sigma(\delta_y^2 + \alpha_{21}^2\delta_x^2)) + \Sigma\delta_x^2\Sigma\delta_y^2 \\ \sigma_{y/x}^2 &= (\sigma_{Fy/x}^2 + \Sigma(\delta_y^2 + \alpha_{21}^2\delta_x^2) + \Sigma\delta_y^2\Sigma\delta_x^2/\sigma_F^2) \cdot (1 + \Sigma\delta_x^2/\sigma_F^2)^{-1} \end{aligned} \quad \text{(C.19)}$$

Let us compare $\sigma_{y/x}$ with the previous noise estimator in 17.

$$\|C'\|_{22} = \|C_F'\|_{22} + \frac{\Sigma\alpha^2\delta_x^2 + \delta_y^2}{1 + \alpha^2} \approx \frac{\sigma_{y/x}^2}{1 + \alpha^2} \quad \text{(C.20)}$$

The comparison shows that if the fringing amplitude σ_F is large compared to the noise δ_x (using filter α and constant level runs at mid range) the two estimators are equivalent. This is checked experimentally. In this case the advantage of conditional law estimators over subtracted images is that no a priori knowlege of gain×flux factor is needed because it is determined in the same go by the slope measurement.
The equations 19 and 20 have an intuitive meaning. They express the RMS dispersion of *Y* (or *X*) at a given *X* (or *Y*) as a quadratic average of the *Y* (or *X*) dispersions due to fringing (cf. eq.13) and to electronics, plus the *X* (or *Y*) dispersion due to electronics projected on the y axis by the y/x slope coefficient. The second order term is neglected. There are too many free parameters in the general model of 18 to analyse the data without adding some constraints. For the case of constant level images presented below we assume that δ_y/δ_x is equal to one and make some approximations to merge the fringing noise and the electronic noise. Then we prove that local differential linearity slope is equal to integral linearity slope. For level ramp exposures the noise ratio δ_y/δ_x between two images is not known a priori as recalled in 15 but we can use linearity as a constraint.

3. Comparing identical images with identical noise

The regression analysis resulting in 18, after replacing the fringing noise term ρ_F by its expression in 13 yields an estimation $\alpha_{y/x}$ for the image 2 over image 1 ratio α_{21} :

$$\frac{\alpha_{y/x}}{\alpha_{21}} = \left(1 - \frac{\sigma^2_{Fy/x}}{\alpha^2_{21}\sigma^2_F}\right)^{1/2}\left(1 + \sum\frac{\delta^2_x}{\sigma^2_F}\right)^{-1} \approx 1 - \frac{1}{2}\left[\frac{\sigma^2_{Fy/x}}{\alpha^2_{21}\sigma^2_F} + 2\sum\frac{\delta^2_x}{\sigma^2_F}\right] \qquad \text{(C.21)}$$

The two terms in the brackets on the right part of 21 are equal to the $\sigma_{y/x}$ estimator given in 19 when the δ_x and δ_y terms are equal. The formula is checked in Figure 36. It

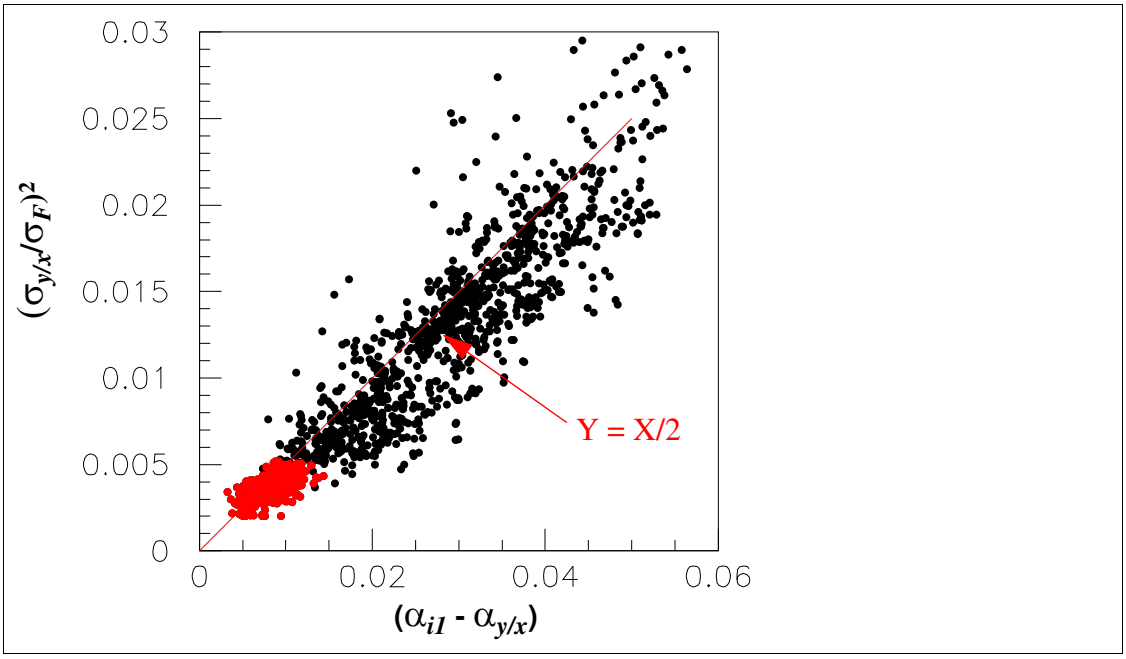

Figure 36: For all 72 channels, the relation between the fluctuation of pixels from image (i) to the reference image (25) and the slope $\alpha_{y/x}$ of the conditional law is expressed in 21. In case of almost identical images the last two terms of 21 are approximately equal to $(\sigma_{y/x}/\sigma_F)^2/2$ from 19. The dispersion seen around this value is 4.10^{-4}. The 10 last images with mostly electronic noise are shown in red. The 14 first images much larger noise due to fringing are seen in black.

yields for all 72 preamps and 25 images a global dispersion of the differential linearity slope ($\alpha_{y/x}$+0.5*$\sigma_{y/x}$**2) of 4.10^{-4} around the integral linearity slope α_{i1} which is measured on a 10 times larger lever arm (20000 adu instead of 1000 adu for a point to point precision of the order of 1 adu). One should remember that the integral electronic gain is varying from one image to the next by a few per mil. At least differential gain is following it!

4. comparing images in a flux ramp :

The aim of this paragraph is to show how we overcome this problem by using four spatial frequency halving operators :
The matrix element $f_{i,j}$ is the expected value of the content of the pixel in column i and line j. It can be considered as a discrete time sampling of the continuous «contrast» function f(x,y) at the node (x_i, y_j) of a rectangular network. The sampling of $f_{i,j}$ is governed by Poisson statistics of N photons. It is approximated by a gaussian law of

mean value $f_{i,j}= \alpha N$ and width $\sigma_{i,j}= \alpha\sqrt{N}$. The non reproductibility of the sndice-megacam imaging can be represented by an auxiliary random «discrepancy» function δf(x,y) which expected value on a sequence of «identical» images is null.
The role of the derivative operators in this problem is to yield derivative images with a much reduced contrast as compared with the original images. The ultimate hope is to be able to neglect the derivative of the discrepancy in comparison with the Poisson noise.
Practically the derivative operators Δ are part of a (Σ, Δ) doublet which creates a reversible operation yielding two images while halving the number of lines (or columns). In order to conserve an x*y symmetry we use the product $(\Sigma, \Delta)_x \times (\Sigma, \Delta)_y$. Each image yields four images with half the number of lines and half the number of columns, namely: $\Sigma_x \times \Sigma_y$; $\Delta_x \times \Sigma_y$; $\Sigma_x \times \Delta_y$; $\Delta_x \times \Delta_y$. Each pair of consecutive images yields 8 images, respectively the four sums and the four differences of the four previous ones).
The essential point for the analysis of photo-electron statistics is the fact that each corresponding pixels in these eight images follow the same Poisson statistics[12].
We can test that hypothesis using three criteria:

A- the gaussiannity of the pixel difference distribution for each channel and each slice

B- the nullity of the mean value of gaussians

C- the evolution of the width of the gaussians as a $\sqrt{N}$ function of the slice (N is the average number of photo-electron per pixel in a given slice)

The first two criteria are visualized in Figure 24 and the third in Figure 37-a.

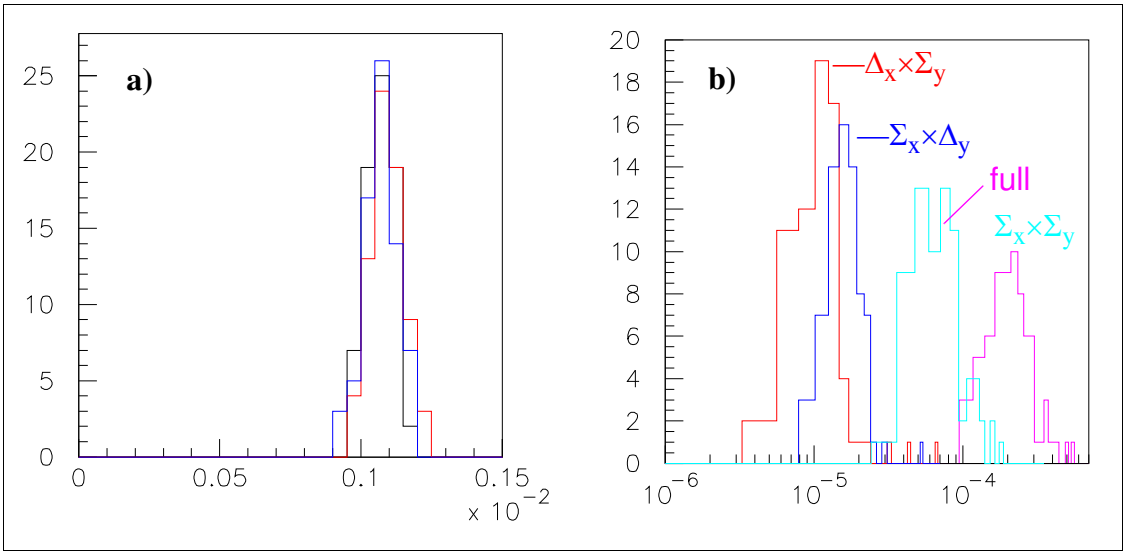

Figure 37: a) Criterion C :Distributions of the derivative of the gaussian width as a function of the charge collected in a pixel for the three "good" operators (— $\Delta_x \times \Delta_y$; —$\Delta_x \times \Sigma_y$ and —$\Sigma_x \times \Delta_y$) applied to the 72 channels
b) The positive value of the excess RMS width drawn here $\sigma(\Delta_x \times \Sigma_y) - \sigma(\Delta_x \times \Delta_y)$; $s(\Sigma_x \times \Delta_y) - \sigma(\Delta_x \times \Delta_y)$; $\sigma(\Sigma_x \times \Sigma_y) - \sigma(\Delta_x \times \Delta_y)$; $\sigma(\text{full}^a) - \sigma(\Delta_x \times \Delta_y)$ confirms that $\Delta_x \times \Delta_y$ is the best Poisson noise estimator

a. the full image estimate of Figure 18 right. A pixel ratio 1 to 4 yield an extra calibration factor 1/2

[12] they are linear combinations of 8 gaussian variables differing only by the sign of the coefficients

We consider that among the four images produced by the four operator introduced above, three pass the test. They are the three images obtained with derivative operators ($\Delta_x \times \Sigma_y$; $\Sigma_x \times \Delta_y$; $\Delta_x \times \Delta_y$). The fourth one ($\Sigma_x \times \Sigma_y$) is just the original image with a resolution reduced by a factor two. In summary we have 5 estimates for the electronic calibration factor of a channel, three of them being demonstrably better. We have a reason to expect that the doubly differential operator ($\Delta_x \times \Delta_y$) is better than the others : it yields a contrast RMS smaller. The study of gain variations suggests also that it mitigates the effect of different electronic gain unstabilities. The optimality of $\Delta_x \times \Delta_y$ can be checked rigorously by showing that the width of its distribution is minimal. For this purpose Figure 37-b plots for each channel the difference between the width of a given estimator and the minimal one. The intuitive explanation is that the non-Poisson noise is correlated along a CCD line, or independently along a column. Therefore our three best operators suppress either line noise, or column noise, or both.
The conclusion of this study is logically to replace all the estimators of electronic calibration by the best one produced by the $\Delta_x \times \Delta_y$ filter. Conclusions of the short term reproducibility test for SNDICE-Megacam images

In the previous paragraph, by comparing two images taken at one minute interval, we determined the absolute gain of each CCD digitization chain. We compared the 24 pairs of images receiving almost identical integrated fluxes (defined at a $2*10^{-4}$ level as seen in Figure 14). This comparison proved that the electronic gain fluctuates within a few parts per mil from from one image to the next and independently for each channel although the average of all 72 channels is stable.
In order to define a strategy for calibrating and monitoring Megacam with SNDICE at a few 10^{-4th} we still have to know the mid term and long term fluctuations of the camera system and to decouple it from the fluctuations of the telescope system. From what we have already seen, this task would be hopeless with traditional tools such as twilight flat fields and the rest.
But with SNDICE we have to release the constraint of using pair of images taken at one minute intervals and at equal light flux.